New Developments in Transmission Electron Microscopy for Nanotechnology**

By *Zhong Lin Wang**

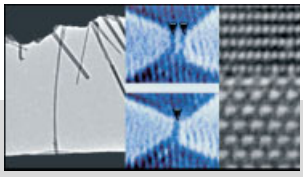

High-resolution transmission electron microscopy (HRTEM) is one of the most powerful tools used for characterizing nanomaterials, and it is indispensable for nanotechnology. This paper reviews some of the most recent developments in electron microscopy techniques for characterizing nanomaterials. The review covers the following areas: in-situ microscopy for studying dynamic shape transformation of nanocrystals; in-situ nanoscale property measurements on the mechanical, electrical and field emission properties of nanotubes/nanowires; environmental microscopy for direct observation of surface reactions; aberration-free angstrom-resolution imaging of light elements (such as oxygen and lithium); high-angle annular-dark-field scanning transmission electron microscopy (STEM); imaging of atom clusters with atomic resolution chemical information; electron holography of magnetic materials; and high-spatial resolution electron energy-loss spectroscopy (EELS) for nanoscale electronic and chemical analysis. It is demonstrated that the picometer-scale science provided by HRTEM is the foundation of nanometer-scale technology.

1. Electron Microscopy and Nanotechnology

Nanotechnology, as an international initiative for science and technology in this century, is a focused area of current research. Advanced nanomaterials and advanced manufacturing are the foundation of nanotechnology. Tracking the historical background of why nanotechnology and why now, it is believed that the following facts may contribute to this global initiative.[1] First, the road map for microelectronics and microsystems will be reaching its limit in about 10 years. As the size of interconnects is thinner than 100 nm and one electron can ignite the switching of a device (so called single electron device), quantum mechanical phenomena are becoming appreciable and dominant. Nanoscale technology is not simply a miniaturization in sizes, but an in-depth revolution in physical concepts, system design, and materials manufacturing. Philosophically, a change in quantity results in a change in quality. Secondly, the development of transmission electron microscopy and scanning probe microscopy allows direct imaging of atomic structures in solids and on surfaces, and these powerful tools provide the "eyes" and "hands" for imaging and manipulating the nanoscale world, fulfilling the dream of moving atoms "one-by-one". This provides a unique opportunity for designing, modifying, and constructing nanoscale structures. Third, the newly discovered nanostructures, such as carbon nanotubes, quantum dots, semiconducting oxide nanobelts, etc. display the diversity and richness of the nano-scale world.[2] The unique, novel, and largely improved properties demonstrated by these structures have illustrated a blue print for the next technological revolution in human civilization. Finally, the powerful modeling techniques and supercomputers can predict possible phenomena that could be realized experimentally, providing guidance in materials design and system analysis.

High-resolution transmission electron microscopy (HRTEM) is one of the most powerful tools used for characterizing nanomaterials, and it is indispensable for nanotechnology.[2] In fact, decades before the national nanotechnology initiative, scientists had started examining "small particles" (nowadays these are called "nanoparticles") by HRTEM. It was not until the early 1990s that inventions of various types of scanning probe microscopy allowed scientists to manipulate at the nanoscale. Traditionally, HRTEM has been mainly applied for imaging, diffraction, and chemical analysis of solid materials.[3] Carbon nanotubes, for example, were first identified by HRTEM.[4,5] Analysis of such tubular structures requires extensive development of electron microscopy, which has been covered very comprehensively in the book edited by Wang.[6] Conventional imaging and diffraction are the two most powerful methods in characterizing the phase structure and phase transformation of inorganic materials. With the assistance of energy dispersive X-ray spectroscopy (EDS) and electron energy-loss spectroscopy (EELS), the transmission electron microscope is a versatile and comprehensive analysis tool for characterizing the chemical and electronic structure at nano-

[*] Prof. Z. L. Wang
School of Materials Science and Engineering
Georgia Institute of Technology
Atlanta, GA 30332-0245 (USA)
E-mail: zhong.wang@mse.gatech.edu

[**] The author is grateful to his collaborators: Drs. Xuedong Bai, Ruiping Gao, Enge Wang, Yolande Berta, Christopher Ma, and Mostafa El-Sayed. Thanks the financial support from NSF and NASA (URETI) and NSFC.

 DOI: 10.1002/adma.200300384

scale.[7] HRTEM has been extensively applied to determine the shape of nanoparticles[8–10] and structures of nanotubes.[6]

In recent years, a number of new and novel developments have been made in HRTEM for nanotechnology, such as in-situ microscopy for observing dynamic processes at nanoscale, nanomeasurement techniques that directly correlate physical properties with structures, holographic imaging of electric and magnetic fields, quantitative chemical mapping at sub-nanometer resolution, and ultra-high resolution imaging techniques. In consideration of the large diversity and amount of literature available in electron microscopy, instead of giving a vast review about HRTEM, this article reviews only the novel developments that have been made in the last few years for solving the problems in nanotechnology. Readers who are interested in fundamentals of TEM are referred to existing text books.[11–13]

2. In-Situ Microscopy

In-situ microscopy refers to the techniques that allow a direct observation of the dynamic properties at the nanoscale through imaging and diffraction. The most traditional in-situ technique is thermal induced structural transformation and transition. More recent developments include in-situ property measurements of nanotubes/nanowires, electric transport through a nanotube, and environmental microscopy.

2.1. Thermally Induced Surface Dynamic Processes of Nanocrystals

In-situ study of the temperature induced phase transformation and the structural and chemical evolution of nanocrystals is important for understanding the structure and structural stability of nanomaterials. TEM is an ideal approach for conducting this type of experiments, in which a specimen can be cooled down to the temperatures of liquid nitrogen or liquid helium or heated to 1200 °C. The in-situ process can be recorded at TV rate for exhibiting the time and temperature dependent phenomena.

The large percentage of surface atoms in nanocrystals is the origin of their unique properties. The melting point of a nanocrystal is much lower than the bulk melting temperature.[14] Here, the melting of Pt particles is taken as an example.[15] Platinum nanoparticles with a high percentage of cubic-, tetrahedral-, and octahedral-like shapes, respectively, have been synthesized by changing the ratio of the concentration of polymer capping material (polyacrylate) to that of Pt^{2+} ions being reduced by H_2 from K_2PtCl_4 at room temperature.[16] Cubic and tetrahedral are the two most typical shapes for the Pt nanocrystals. We now apply in-situ TEM to determine the stability of particle shapes and the melting behavior.

Figure 1 shows a series of TEM images recorded from the same region when the specimen temperature was increased from 25 to 610 °C. These images were selected from a group of images to present the most significant changes in particle shape. For easy notation, particles are labeled as groups to track their shape transformation behavior. Most of the particle shapes showed no significant change when the specimen temperature was below 350 °C (Figs. 1a–c). Truncated cubic and tetrahedral particles were formed when the temperature reached 410 °C (Fig. 1d). The corners and edges of the particles were disappearing because these local atoms have a higher energy. The tetrahedral particles could still be identified even when the temperature reached 500 °C (Fig. 1e), while the cubic particles became spherical when the temperature was above 500 °C. This indicates that the tetrahedral particles are more stable than cubic ones, possibly because the {111} surfaces have lower surface energy than the {100}. A feature observed in Figure 1 is that the tetrahedral shape of a particle labeled as T_1 was preserved when the specimen temperature was as high as 610 °C. This is possibly due to the contact of the apexes of the particle with the adjacent particles, so that the interparticle diffusion can still sustain the shape of the apexes. These results indicate that the surface capping polymer is removed by annealing the specimen to a temperature of 180–250 °C, while the particle shape shows no change up to ~350 °C. In a temperature range of 350 to 450 °C, a small truncation occurs in the particle shape but there is no major shape transformation. The particle shape experiences a dramatic

Zhong Lin Wang received his Ph.D. in Physics from Arizona State University in 1987. He is currently a Professor, the Director of the Center for Nanoscience and Nanotechnology, and the Director of the Electron Microscopy Center at the Georgia Institute of Technology. Prof. Wang has authored and co-authored four scientific reference and textbooks and 320 journal articles, edited and co-edited nine volumes of books on nanotechnology, and is amongst the top 20 most cited authors in nanotechnology from 1992 to 2002. He was elected to the European Academy of Science in 2002, and received the 2001 S.T. Li prize for Outstanding Contribution in Nanoscience and Nanotechnology, the 2000 Georgia Tech Faculty Research Award, the 1999 Burton Medal from the Microscopy Society of America, 1998 US NSF CAREER grant award, and 1998 China-NSF Oversea Outstanding Young Scientists Award. He is an associated editor for The European Physical Journal—Applied Physics, member of the editorial board of Micron, Advanced Functional Materials, Journal of Nanoscience and Nanotechnology, and Progress in Natural Science. Prof. Wang's most recent research focuses on oxide nanobelts and nanowires, in-situ techniques for nano-scale measurements, self-assembly nanostructures, fabrication of nanodevices, and properties of magnetic nanostructures.

ADVANCED MATERIALS

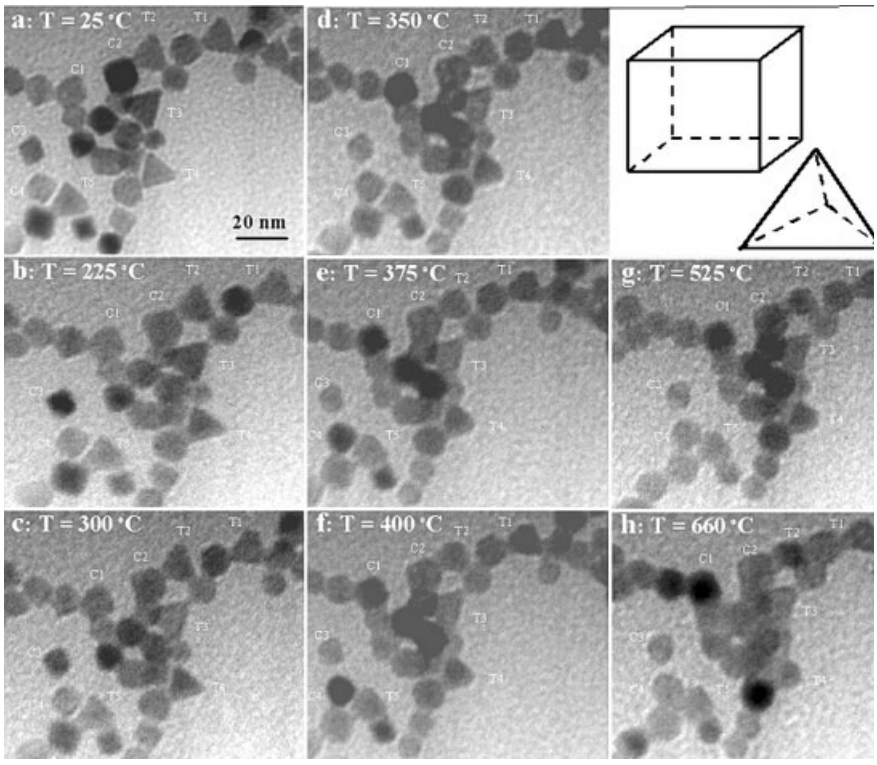

Fig. 1. A series of TEM images recorded in-situ from Pt nanocrystals dispersed on a carbon substrate and heated to different temperatures, exhibiting the shape transformation as well as surface melting phenomenon of the particles at temperatures much lower than the melting point of the bulk. Models for cubic and tetragonal polyhedra are also shown.

transformation into spherical-like shape when the temperature is higher than ~500 °C (the melting point of bulk Pt is 1773 °C).

Using the confined and unique geometry provided by nanomaterials, other interesting experiments have been carried out using in-situ TEM. Gao and Bando[17] have demonstrated a nanothermometer in TEM. By trapping liquid gallium in a closed carbon nanotube during the nanotube growth, the volume/height of the gallium liquid increases as the temperature increases, forming a nanothermometer.

2.2. In-Situ Measurement of Mechanical Properties of Nanotubes/Nanobelts/Nanowires[18]

Cantilever-based sensors present wide range applications in the field of physical, chemical, and biochemical sciences,[19–21] which are based on the bending induced by the surface adsorbed foreign molecules as a result of changes in surface energy. The most conventional cantilevers are based on Si, SiC, or SiN, with a typical length of 50 μm, width of 5 μm, and thickness of 0.5 μm. Miniaturization of the cantilever dimensions toward the nanometer scale will enable an improvement in sensitivity, spatial resolution, energy efficiency, and time of response.[22,23] Semiconducting oxide nanobelts[24] and nanowires,[25] as a new class of nanostructures, are showing novel electronic, chemical, and optical properties.[26,27] Nanowires are the fundamental building blocks for fabricating nanoscale sensors and logic circuits.[28,29] Recently, nanobelts of semiconducting oxides have been synthesized using a solid–vapor process.[24] The nanobelts have a distinct structural morphology, characterized by a rectangular cross-section and a uniform structure, which could be directly used as nanocantilevers andnanoresonators in nanoelectromechanical systems (NEMS).[30,31] A key phenomenon for applying nanobelts in NEMS technology is their electromechanical resonance behavior, and an important physical quantity for cantilever applications is their bending modulus.

Measurement of the bending modulus of a nanowire/nanotube/nanobelt object with a length of a few micrometers is rather challenging because its small size prevents the application of the established techniques for mechanical testing. Recently, a new experimental approach, based on the electric-field-induced resonant excitation, has been developed for direct measurement of the mechanical properties of individual nanowire-like structures by in-situ TEM.[32,33] Using this method, mechanical properties of carbon nanotubes[32,34] and silicon carbide-silica composite nanowires[35] have been investigated. Here the application of this technique is demonstrated for studying the resonance behavior of a nanobelt.[36]

To carry out property measurements of a nanobelt, a key step is to design and build a specimen holder that can apply an electric field across nanostructures. The specimen holder requires the translation of the nanobelt via either mechanical movement by a micrometer or axial directional piezo. The static and dynamic properties of the nanobelt can be obtained by applying a controllable static and alternating electric field. Figure 2a shows a typical TEM image of the ZnO nanobelt, displaying high structural uniformity. The selected area electron diffraction pattern indicates that the nanobelt grows

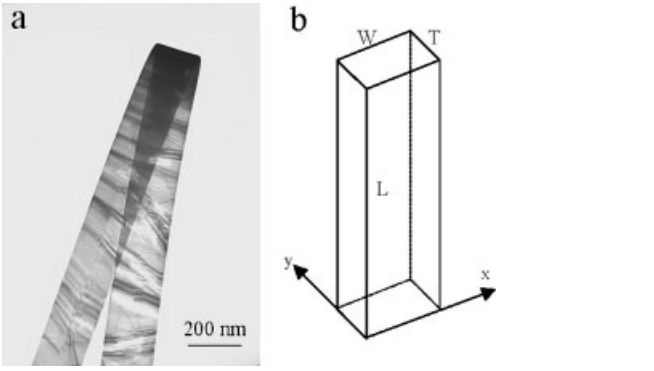

Fig. 2. a) A typical TEM image of a ZnO nanobelt. b) Schematic geometrical shape of a nanobelt.

along [0001] and is enclosed by $\pm(2\bar{1}\bar{1}0)$ and $\pm(01\bar{1}0)$ facets.[24] Figure 2b represents the geometry of a nanobelt with length L, width W, and thickness T. In our experiment, the nanobelts were glued at one end onto a copper wire, while the other end near the counter electrode was free. This is a simple one-end clamped cantilever with a rectangular cross section. An oscillating voltage with tunable frequency was applied to the nanobelt. Mechanical resonance of the nanobelt can be induced if the applied frequency matches the natural vibration frequency (Fig. 2). From the classical elasticity theory for a rectangular beam,[37] the fundamental resonance frequency corresponding to the thickness direction (x-axis) (Fig. 2c) is

$$\nu_{xi} = \frac{\beta_i^2 T}{4\pi L^2}\sqrt{\frac{E_x}{3\rho}} \quad (1)$$

where β_i is a constant for the ith harmonic: $\beta = 1.875$ and $\beta_2 = 4.694$, E_x is the bending modulus for the vibration along the x-axis, L is length of the nanobelt, ρ is the mass density; and the corresponding resonance frequency in the width direction (y-axis) (Fig. 2c) is given by

$$\nu_{yi} = \frac{\beta_i^2 W}{4\pi L^2}\sqrt{\frac{E_y}{3\rho}} \quad (2)$$

A selected ZnO stationary nanobelt is given in Figure 3a. By changing the frequency of the applied voltage, we have found two fundamental frequencies in two orthogonal transverse vibration directions. Figure 3b shows a harmonic resonance with its vibration plane nearly parallel to the viewing direction, and Figure 3c shows the harmonic resonance with the vibration plane closely perpendicular to the viewing direction. For calculating the bending modulus, it is critical to accurately measure

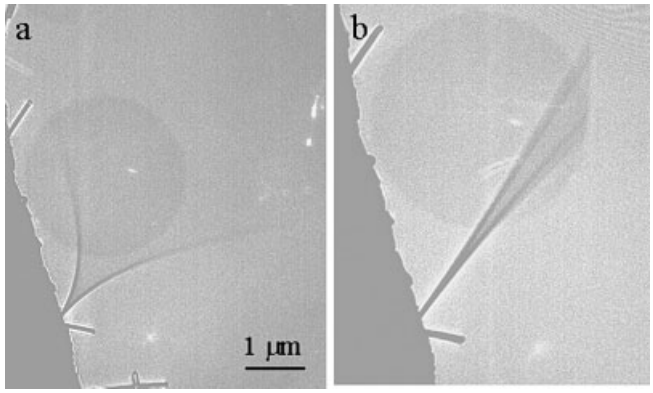

Fig. 3 Electromechanical dual-mode resonance of a ZnO nanobelt: a) closely perpendicular to the viewing direction ($\nu_x = 1.25$ MHz), b) nearly parallel to the viewing direction ($\nu_x = 1.38$ MHz).

the fundamental resonance frequency (ν_1) and the dimensional sizes (L, W, and T) of the investigated ZnO nanobelts. Based on the experimentally measured data, the bending modulus of the ZnO nanobelts is calculated using Equation 1 and Equation 2. The experimental results are summarized in Table 1. The bending modulus of the ZnO nanobelts was ~52 GPa. This value represents the modulus that includes the scaling effect and geometrical shape, and it is in excellent agreement with the elastic modulus measured by a nanoindenter.[21] Although nanobelts of different sizes may have slight difference in bending modulus, there is no obvious difference if the calculation was done using either Equation 1 or Equation 2. The ratio of two fundamental frequencies ν_{y1}/ν_{x1} is consistent with the aspect ratio W/T, as expected from Equation 1 and 2 ($\nu_{y1}/\nu_{x1} = W/T$ if $E_x = E_y$). The nanobelts could be used as a new type single crystalline nanoresonator and nanocantilever with dual operation modes, which could be useful in nanoelectromechanical systems and highly functional nanodevices.

Other in-situ mechanical testing, such as stretching and nano-indentation have also been observed by in-situ TEM.[38] The failure modes of carbon nanotubes under load have been observed by in-situ TEM. Nanoindentation to measure the hardness of a thin film, while the creation and movement of dislocations was observed simultaneously, has also been illustrated.[39] But quantitative calibration of the force applied remains a key challenge. Recently, atomic force microscopy has also been used in conjunction with TEM to study gold–gold interaction, showing the possibility of integrating AFM with TEM.[40]

Table 1. Bending modulus of the ZnO nanobelts. E_x and E_y represents the bending modulus corresponding the resonance along the thickness and width directions, respectively.

	Length L [μm]	Width W [nm]	Thickness T [nm]		Fundamental Frequencies [Gpa]			Bending Moduli [Gpa]	
Nanobelt	(± 0.05)	(± 1)	(± 1)	W/T	ν_{x1}	ν_{y1}	ν_{y1}/ν_{x1}	E_x	E_y
1	8.25	55	33	1.7	232	373	1.6	46.6 ± 0.6	50.1 ± 0.6
2	4.73	28	19	1.5	396	576	1.4	44.3 ± 1.3	45.5 ± 2.9
3	4.07	31	20	1.6	662	958	1.4	56.3 ± 0.9	64.6 ± 2.3
4	8.90	44	39	1.1	210	231	1.1	37.9 ± 0.6	39.9 ± 1.2

ADVANCED MATERIALS

2.3. In-Situ Measurement of the Electric Transport in a Carbon Nanotube[41,42]

Measurements of electric transport in nanotubes usually use the two-point or four-point contact methods, in which the contacting electrodes are fabricated using lithography and the nanotube is laid down onto the electrodes.[43] An alternative method has been developed to measure the nanotube electric transport in TEM.[44] Using the same type of specimen holder as used for mechanical property measurement, by changing the count electrode into a soft contacting metal, such as a tiny mercury droplet, a carbon nanotube can be directly put in contact with the electrode, and thus its transport properties can be measured (Fig. 4). The advantage offered by such a set up is that the nanotube can be directly imaged under the electron beam, while its electrical properties are characterized.

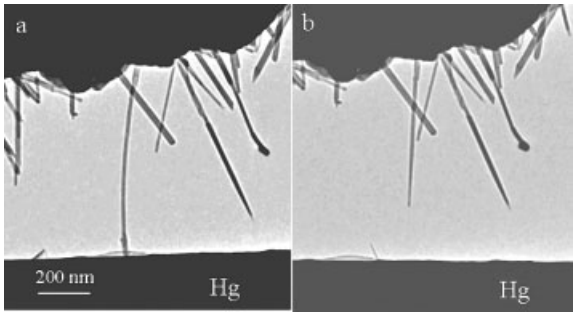

Fig. 4. In-situ observation of electric transport through a single carbon nanotubes. a) Applied voltage $V = 0.1$ V, current $I = 7.3$ μA, the resistance of the carbon $R = 12.7$ kΩ, which corresponds to a conductance $G = (12.7\ \text{k}\Omega)^{-1} = 1.02\ G_0$. b) After applying a 4 V voltage, the nanotube was broken and the break occurred at the contact of the nanotube and the Hg. c) The conductance of this carbon nanotube contaminated with graphitic particles is $0.25\ G_0$.

The contact area between the tube and the mercury can be significantly increased by inserting the nanotube into the mercury, thus, the contact resistance is drastically reduced and becomes negligible. This technique was first accomplished using the tip of an AFM and it demonstrated room-temperature ballistic conductance of a multi-walled carbon nanotube.[45]

The in-situ TEM provides a direct image of the nanotube while the electric properties are being measured. For a multi-walled carbon nanotube, if the applied voltage is a fraction of a volt, the conductance of the nanotube is measured to be close to $(12.7\ \text{k}\Omega)^{-1}$, which is very close to the single chance conductance $G_0 = 2e^2/h = (12.9\ \text{k}\Omega)^{-1}$ predicted by quantum mechanics. For a carbon nanotube without defects, the link between the graphitic sheets is weak, and there is little tunneling effect between the layers if the applied voltage is small. The current is effectively carried by the outmost layer although the nanotube is multi-walled.[45] If the applied voltage is increased to 4 V, the nanotube burned out at the contacting point with the Hg electrode (Fig. 4b). This is due to the contact between the nanotube and the mercury. At such a high voltage, tunneling between graphitic layers is strongly enhanced, thus the entire thickness of the wall would be effective for conducting current. The increased size of the conducting cross-section leads to the disappearance of the quantum conductance effect.

My co-workers and I have previously shown that a defect-free nanotube can be a room-temperature ballistic conductor without heat dissipation.[45] However, at the junction of two nanotubes, defects must be introduced, such as the case shown in Figure 5a, thus, heat dissipation at the defects is possible. After applying a higher voltage, the burning point between the two nanotubes is just the junction point, as shown in Figure 5b. TEM provides powerful evidence for this transport phenomenon.

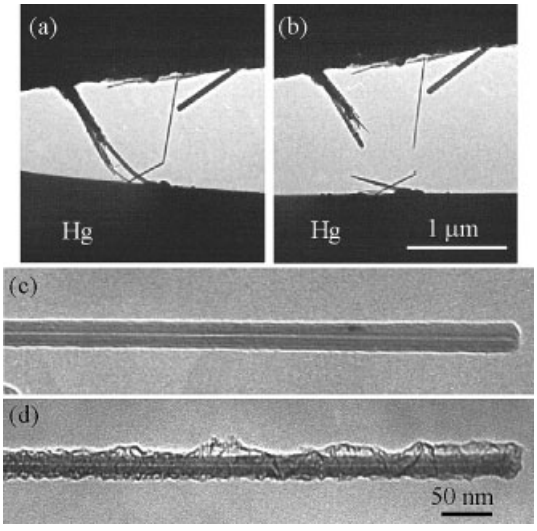

Fig. 5. Examples of nanotube failure modes under applied current. Multi-walled carbon nanotubes a) before and b) after passing a large current, showing the break points at the defect sites. c,d) A nanotube before and after passing a large current through it. In (d) the tip of the nanotube had been contacted to a Au surface and current was passed trough it. Only the outer layer, starting at the contact point has been damaged, suggesting that the current flows over the surface.

The room-temperature ballistic transport of a carbon nanotube was attributed to the single layer conductivity of the nanotube. Graphite has a unique layer structure, in which the conductivity parallel to the graphitic plane (*a*–*b* axis plane) is about 50 times higher than that along the *c*-axis. If the applied voltage is small, so that the interlayer tunneling effect can be ignored and the end of the nanotube is closed, the electric current mainly flows along the top surface layer, provided the tube is perfect and there are no defects. Since the layer thickness of ~0.34 nm is comparable to the wavelength of the conduction electron in the graphitic (~0.5 nm), quantum conductance is possible. Figure 5d shows a multi-walled nanotube after passing a large current, which was brought into contact with an Au surface during the field emission experiments. Due to a flow of a shock short-circuit current, the surface of the nanotube is disrupted starting at the contact point while the interior layers are not visibly affected. This observation provides further evidence that the electronic current passes over the surface layers of the nanotube, e.g., the single layer conductance.

2.4. In-Situ Measurement the Work Function at the Tip of a Carbon Nanotube[46]

An important physical quantity in electron field emission is the surface work function, which is well documented for elemental materials. For emitters such as carbon nanotubes (NTs), most of the electrons are emitted from the tips of the carbon NTs, and it is the local work function that matters to the properties of the NT field emission. The work function measured from the $\ln(J/E^2)$ versus $1/E$ characteristics curve, where E is the macroscopic applied electric field that is an average over all of the aligned carbon NTs that are structurally divers in diameters, lengths, and helical angles, and J is the measured electric current density. We have developed a technique for the measurement the work function at the tip of a single carbon nanotube.[47]

Our measurement is based on the electric field induced mechanical resonance of carbon nanotubes, but with a slight modification. The principle for work function measurement is schematically shown in Figure 6a. We consider a simple case in which a carbon nanotube, partially soaked in a carbon fiber produced by arc-discharge, is electrically connected to a gold

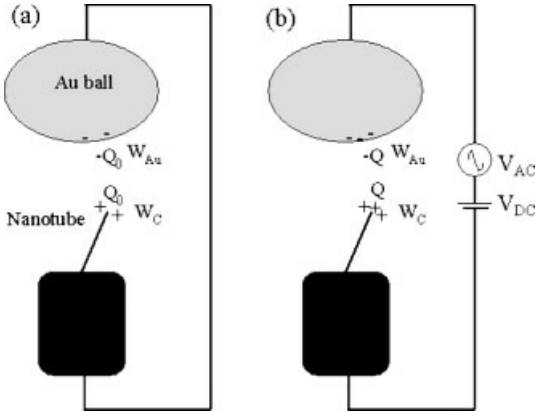

Fig. 6. a) Schematic diagram showing the static charge at the tip of a carbon nanotube as a result of difference in work functions between the nanotube and the gold electrode. b) Schematic experimental approach for measuring the work function at the tip of a carbon nanotube.

ball. Due to the difference in the surface work functions between the NT and the counter Au electrode, a static charge Q_0 exists at the tip of the NT to balance this potential difference even at zero applied voltage.[48] The magnitude of Q_0 is proportional to the difference between the work functions of the Au electrode and the NT tip (NTT), $Q_0 = \alpha(W_{Au} - W_{NTT})$, where α is related to the geometry and distance between the NT and the electrode.

The measurement relies on the mechanical resonance of the carbon NT induced by an externally applied oscillating voltage with tunable frequency. In this case, a constant voltage, V_{DC}, and an oscillating voltage, $V_{AC}\cos 2\pi ft$, are applied onto the NT, as shown in Figure 6b, where f is the frequency and V_{AC} is the amplitude. The total induced charge on the NT is

$$Q = Q_0 + \alpha e(V_{DC} + V_{AC}\cos 2\pi ft) \quad (3)$$

The force acting on the NT is proportional to the square of the total charge on the nanotube

$$\begin{aligned} F &= \beta\,[Q_0 + \alpha e(V_{DC} + V_{AC}\cos 2\pi ft)]^2 \\ &= \alpha^2\beta\,\{[(W_{Au} - W_{NTT} + eV_{DC})^2 + e^2 V_{AC}^2/2] \\ &\quad + 2eV_{AC}(W_{Au} - W_{NTT} + eV_{DC})\cos 2\pi ft \\ &\quad + e^2 V_{AC}^2/2 \cos 4\pi ft\} \end{aligned} \quad (4)$$

where β is a proportional constant. In Equation 4, the first term is constant and it causes a static deflection of the carbon NT; the second term is a linear term, and the resonance occurs if the applied frequency, f, approaches the intrinsic mechanical resonance frequency, f_0, of the carbon NT (Fig. 7a). The last term in Equation 4 is the second harmonics. The most important result of Equation 4 is that, for the linear term, the resonance amplitude A of the NT is proportional to $V_{AC}(W_{Au} - W_{NTT} + eV_{DC})$. By fixing the V_{DC} and measuring the vibration amplitude as a function of V_{AC}, a linear curve is obtained (Fig. 7c).

Experimentally, we first set $V_{DC} = 0$ and tuned the frequency, f, to find the mechanical resonance induced by the applied field. Secondly, under the resonance condition of

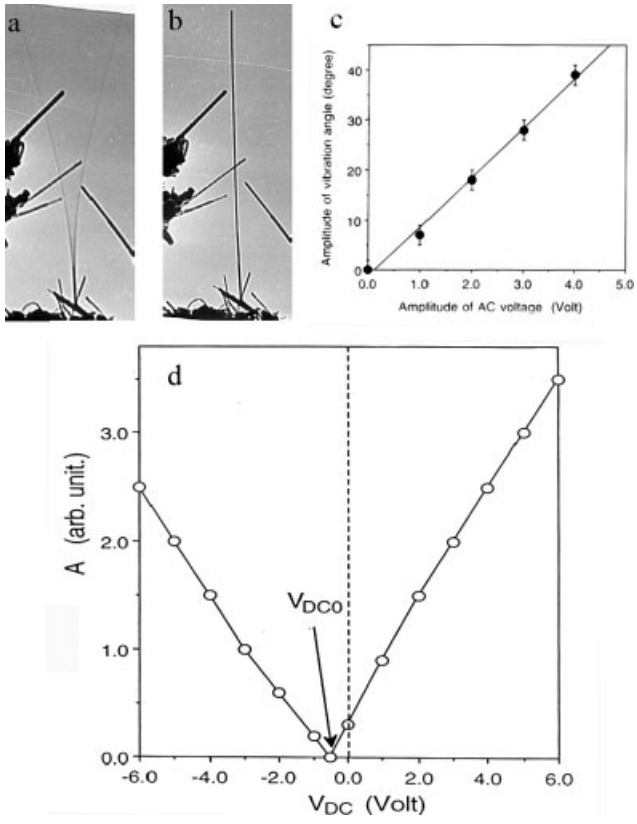

Fig. 7. a) Mechanical resonance of a carbon nanotube induced by an oscillating electric field; b) halting the resonance by meeting the condition of $W_{Au} - W_{NTT} + eV_{DC0} = 0$. c) A plot of vibration amplitude of a carbon nanotube as a function of the amplitude of the applied alternating voltage V_{AC}. d) A plot of vibration amplitude of a carbon nanotube as a function of the applied direct current voltage V_{DC}, while the applied frequency is 0.493 MHz and $V_{AC} = 5$ V.

ADVANCED MATERIALS

keeping $f = f_0$ and V_{AC} constant, slowly change the magnitude of V_{DC} from zero to a value that satisfies $W_{Au} - W_{NTT} + eV_{DC0} = 0$ (Fig. 7b); the resonance amplitude A should be zero although the oscillating voltage is still in effect. V_{DC0} is the x-axis interception in the $A \sim V_{DC}$ plot (Fig. 7). Thus, the tip work function of the NT is $W_{NTT} = W_{Au} + eV_{DC0}$. Our data show that most of the nanotube tips have a work function of 4.6–4.8 eV, lower than the work function of carbon ($W_C = 5.0$ eV).[47]

The technique demonstrated above, in principle, can be applied to measure the work function at tips of any nanowires, conducting, semiconducting, or insulating. We have applied the technique to measure the work function at the tips of ZnO semiconducting oxide nanobelts.[49] We found that the work function is very sensitive to the surface structure at the tip. A small metallic layer at the tip could significantly reduce the tip work function.

For multi-walled carbon nanotubes, the bonding between the shells is van der Waals, thus the inter-wall linkage is rather weak. Therefore, sliding between the walls is possible. By opening one end of a nanotube, carbon nanotubes can be used as ultralow-friction nanoscale linear bearings and constant-force nanosprings.[50] The inner walls can be repeatedly, reversibly pulled out by the electrostatic force and self-sucked in. Repeated extension and retraction of telescoping nanotube segments revealed no wear or fatigue on the atomic scale as revealed by in-situ TEM.

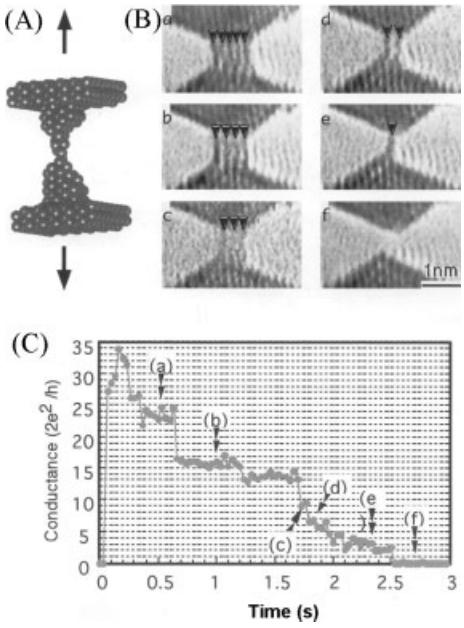

Fig. 8. A) Schematic diagram showing the mechanical stretching of atom-wire by a scanning tip in TEM. B) High-resolution TEM images showing the gold nanowires with widths of a) five, b) four, c) three, d) two, e) one, and f) zero (broken) atom columns, created by mechanical stretching. C) Corresponding measurement of the electrical conductance across the wire as shown in (B) as a function of the stretching time, showing quantum conductance (Images courtesy of Prof. K. Takayanagi, Tokyo Institute of Technology).

2.5. Transport Through a Molecular Nanowire

Introducing STM into TEM was first demonstrated by Spence and co-workers,[51] aiming at improving the resolution for imaging surfaces using reflected electron microscopy.[52] This approach has been extensively developed in recent years for nanotechnology. Takayanagi and co-workers have applied the technique to study molecular nanowires in an ultra-high vacuum TEM. They used a gold wire as the tip of the STM, which is directly in contact with a gold counter electrode. A slow retraction of the tip results in the formation of Au molecular nanowires of a few atoms in thickness. The electric current passing through the nanowire is monitored simultaneously while the nanowire is stretched, providing one-to-one correspondence between the structure and the conductance of the nanowire.[53,54] They have observed the structural transformation from a six-prism to a helical multi-shell tubular structure if the diameter of the gold nanowire is less than 2 nm. The conjunction application of high-resolution TEM and STM was successfully demonstrated for correlating atomic structure with nanoscale properties.

Figure 8A shows a schematic diagram of creating an atom-wire by mechanical stretching in TEM. The gold atom-wires with widths of a) five, b) four, c) three, d) two, e) one, and f) zero (broken) atom columns are shown in Figure 8B. These images show the first direct observation of atom-wires to thickness of one atomic column. The corresponding measurement of the electrical conductance across the atom-wire while being stretched is given in Figure 8C. The conductance plateaus measured as the wire thickness is reduced are marked in correspondence with the wire thickness indicated in Figure 8B, which are given in the unit of $Q_0 = 2e^2/h$, the single channel conductance predicted by quantum mechanics. In the cases of (a–c), the conductance Q is measured to be 25, 16, 9 Q_0, corresponding to atom columns of $5 \times 5 = 25$, $4 \times 4 = 16$, and $3 \times 3 = 9$, respectively. For the case of (e), the measured conductance changed from $4Q_0$ to $2Q_0$, which might have resulted from the shrinkage of the atomic columns from two to one if they were aligned in the direction parallel to the incident electron beam direction.

Ugarte and co-workers[55] have also carried out similar experiments using a conventional TEM. They have thoroughly analyzed the dynamical structural evolution of Au, Ag, and Pt nanowires due to mechanical stretching. Atomically resolved images have revealed that just before rupture, nanowires are crystalline and free of defects and have only a reduced number of structures whose formation is determined by surface energy (faceting pattern).[56] The structural information derived from HRTEM observations was essential to understand the variable conductance behavior of nanowires generated by mechanical stretching. These results emphasize the need of considering an atomic description when analyzing the transport properties of nanoscopic systems.

2.6. In-Situ Environmental Microscopy for Observing Gas–Liquid-Nanoparticle Interaction

Structural analysis in TEM is always carried out in vacuum, typically 10^{-8} torr. It is possible that surface processes occurring in high vacuum are very different from those in gaseous or wet environments, thus, it is very possible that the dynamic surface process revealed by TEM may not be the realistic picture of a practical reaction. It is known that catalytic activities on heterogeneous catalysts occur entirely at the surface under ambient conditions. It has been a long time dream to develop a microscopic technique that can image surface processes and catalytic behavior on nanoparticles in-situ in a more realistic gaseous environment. But the technical difficulty is that the gas molecules near the sample would collide with the incident electrons, producing a diffuse scattering pattern, and thus the image resolution would be greatly reduced.

Great progress has been made in recent years in developing environmental transmission electron microscopy. An environmental cell is built around the objective lens that contains the specimen in a lower pressure gas environment. The electron beam enters the cell through a tiny hole, outside of which a powerful pumping system is designed to maintain the required vacuum for operating the electron source. Instrumental design allows imaging, diffraction, spectroscopy, and chemical mapping to be carried out in-situ simultaneously using the environmental TEM.[57] Gas-catalysis reactions can be directly observed in-situ at sub-nanometer resolution.[58] This technique has been extended to a wet cell for directly observing liquid-catalyst reactions at the operating temperature at nanometer scale.[59] Dynamic liquid hydrogenation and polymerization reactions in the manufacture of polyamides have been imaged directly, opening up the possibility of electron microscopy in a wet environment.

Figure 9 shows an in-situ liquid-catalyst reaction process and the production and growth of the linear polyamide nylon-6,6.[59] The liquids are amidic acid and hexamethylene diamine (HMD) and the catalyst is Ru-Co on titania (m). The reaction temperature in Figure 9b is 188 °C, and the formation of polyamide nylon-6,6 is directly observed. This is an outstanding example that shows the true reaction process at operating temperatures of the catalyst.[60]

Direct observation of the location, state, and function of a promoter in heterogeneous catalysis is critical in understanding the surface processes in catalysis. Hansen et al.[61] has recently achieved atomic resolution (0.14 nm) in-situ imaging of nanoparticles exposed to reaction gases at elevated temperatures. In the most active barium-promoted ruthenium catalyst for ammonia synthesis, through in-situ TEM observation at 552 °C and 5.2 mbar in a gas composition of H_2/N_2 of 3:1, they suggest that the increased activity is related to a two-dimensional barium-oxygen over-layer on the Ru crystals. A dynamic shape change of the supported copper nanocrystals has been revealed at atomic resolution.[62]

Figure 10 shows the high-resolution TEM image Cu nanocrystals supported on ZnO substrate at pressures of 1.5 and

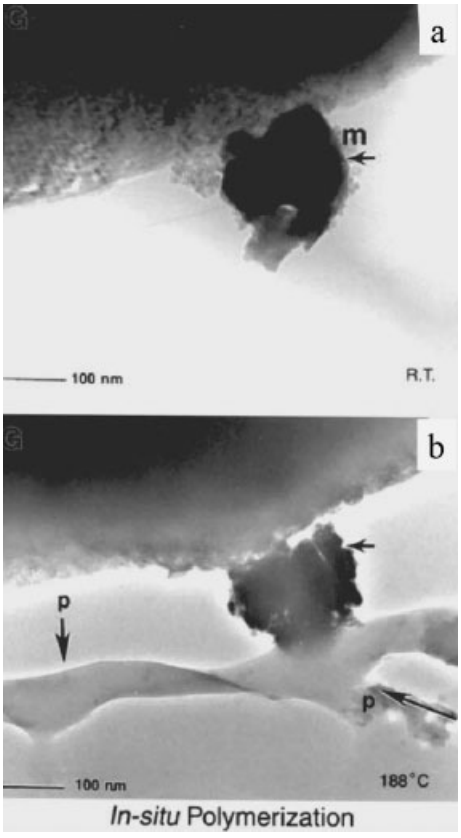

Fig. 9. In-situ TEM imaging of liquid-catalyst reaction processes and the production and growth of the linear polyamide nylon-6,6. The liquids are amidic acid and hexamethylene diamine (HMD) and the catalyst is Ru-Co on titania (m). The reaction temperature in is 188 °C (Image courtesy of Dr. Pratibha L. Gai, Du Pont R&D)

5.0 mbar in a composed gas environment at $T = 220$ °C.[62] The particle shapes can be identified through the lattice images observed directly. For face-centered cubic (fcc) structured metals, the surfaces of the particles can be described by the Wulff construction with the inclusion of {111}, {100}, and {110} types facets. The proportions of the {100} and {110} are significant at 1.5 mbar pressure, while these faces are greatly reduced after the pressure increases to 5 mbar. The change in the crystal facets surrounding the particles significantly affects their catalytic behavior.

3. Quantitative Chemical Imaging at Sub-Nanometer Resolution

Although high-resolution TEM imaging is powerful for directly observing atomic structures of nanomaterials, the image contrast is not very sensitive differences in atomic number, and in cases of light elements, such as oxygen, the weak scattering of the atom results in vanishing contrast. To quantitatively determine the structure of nanomaterials, chemical analysis at spatial resolutions of sub-nanometers or approaching angstrom is critical in solving many material problems. There are two techniques for chemical analysis in TEM: EDS

ADVANCED MATERIALS

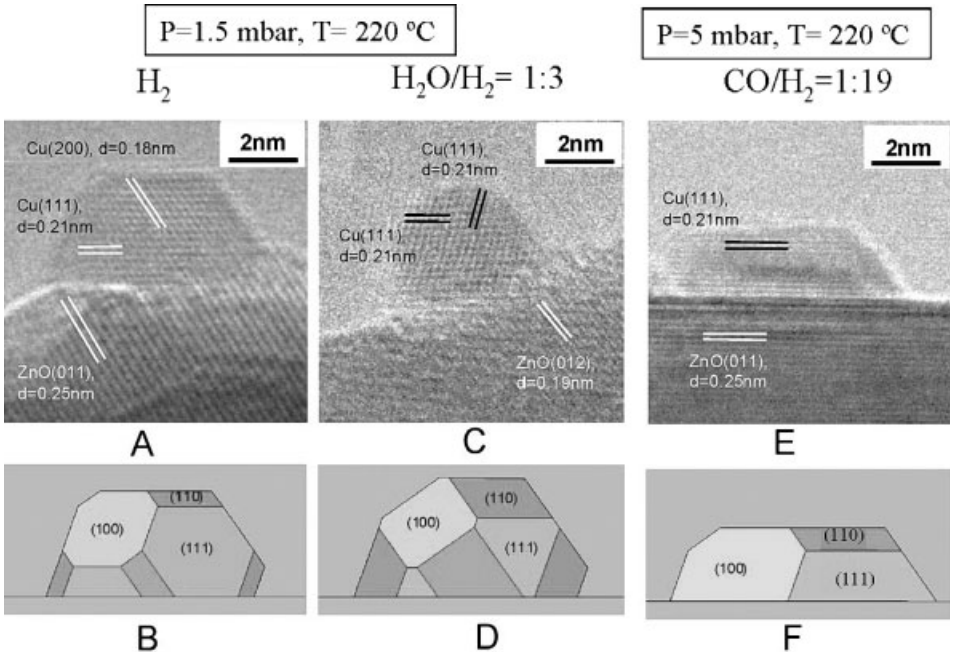

Fig. 10. In situ TEM images (A,C,E) of a Cu/ZnO catalyst in various gas environments together with the corresponding Wulff constructions of the Cu nanocrystals (B,D,F). A) The image was recorded at a pressure of 1.5 mbar of H_2 at 220 °C. The electron beam is parallel to the [011] zone-axis of copper. C) Obtained in a gas mixture of H_2 and H_2O, $H_2/H_2O = 3:1$ at a total pressure of 1.5 mbar at 220 °C. E) Obtained in a gas mixture of H_2 (95 %) and CO (5 %) at a total pressure of 5 mbar at 220 °C (Image courtesy of Dr. P. L. Hansen et al., with permission from AAAS).

and EELS. Due to the small thickness of samples used for TEM, the spatial resolution of the chemical analysis is approximately determined by the size of the electron probe, which can approach 0.1 nm. The thickness-projected elemental maps can be obtained by collecting the characteristic signals while the electron probe is scanned across a sample in a scanning transmission electron microscope (STEM). This is a well-established technique for chemical mapping.

There are two important developments in microanalysis in the last few years. Using the newly corrected electron optical system (see Sec. 5) and the high-coherence, high-brightness field-emission electron source, an electron probe with a diameter as small as ~0.1 nm has been achieved. Such a fine electron probe is ideal for probing the chemical and electronic structure of a sample, atomic column by atomic column, providing the most powerful analytical technique for nanotechnology research. The other key advance is the improvement of energy resolution in TEM/STEM, so that electronic structure mapping can be performed. We use the following examples to illustrate the advances in these two major areas.

The analysis of multi-walled C-BN nanotubes is an example. Tubular structures can be formed by either a rolling graphitic layer or a BN layer. Arc-discharging a mixture of carbon and BN produces composite C-BN nanotubes. The structures of the C-BN nanotubes cannot be distinguished from carbon nanotubes using high-resolution TEM because there is no significant difference of the scattering from B or N compared to that of carbon. Chemical mapping using a fine electron probe is unique for this type of study. By collecting the EELS spectra of the transmitted electron beam, while the electron beam is scanned across the diameter of the tube, a group of thickness-projected chemical compositions of the sample is recorded (Fig. 11).[63] The layers of the tubes have various chemical compositions. Besides the typical case of

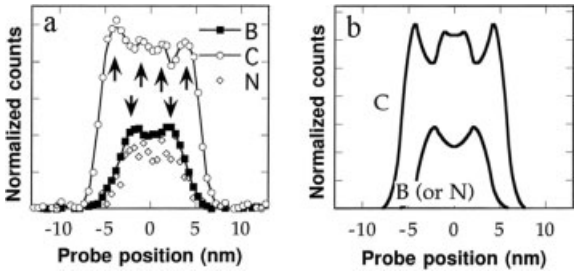

Fig. 11. Composite nanotube with the C-BN-C sandwich structure. A) TEM image showing the graphitic-like structure. B) Elemental profiles measured across a tube similar to that shown in (A); the arrows indicate the anticorrelation between C and B (or N). C) Simulated profiles for C and B (or N) distributions for the coaxial heterostructure shown in (D) (Courtesy of Dr. K. Suenaga and Dr. C. Colliex, University of Paris-Sud).

pure BN tubes, all tubes were found to have well-separated BN layers and carbon layers. From the concentration profiles taken across such a tube, the presence in the carbon profile of four maxima and two minima coinciding with the two maxima of the B and N profiles clearly indicates an alternating C-rich-BN-rich-C-rich geometry (Fig. 11a). These profiles were simulated for various distributions of layers with different chemical compositions (Fig. 11b). The best agreement with experiment was obtained in this case for a 14-layer tube, 12 nm in external diameter, formed with three inner layers of graphitic carbon covered by six $(BN)_xC_{2y}$ layers (with $y/x \sim 0.05 \pm 0.05$) and five outer carbon layers. Chemical mapping using EELS has also been applied to directly imaging the presence of a single Gd atom trapped inside C_{60} molecules (the peapod structure).[64] The data give unambiguous proof of the proposed model.

To illustrate the application of high-spatial resolution EELS, we use the Cu–Al_2O_3 interface to be presented in Figures 20 and 21 as an example. Figure 12 shows the Cu L-edge

EELS spectra acquired from the Cu film and from the region containing the Cu–Al_2O_3 interface using an electron probe of ~0.5 nm in size.[65] The difference spectrum is received by subtracting the EELS spectrum acquired from the Cu side from that from the interface region with a proper scaling factor. The interfacial Cu L-edge shows a chemical shift of

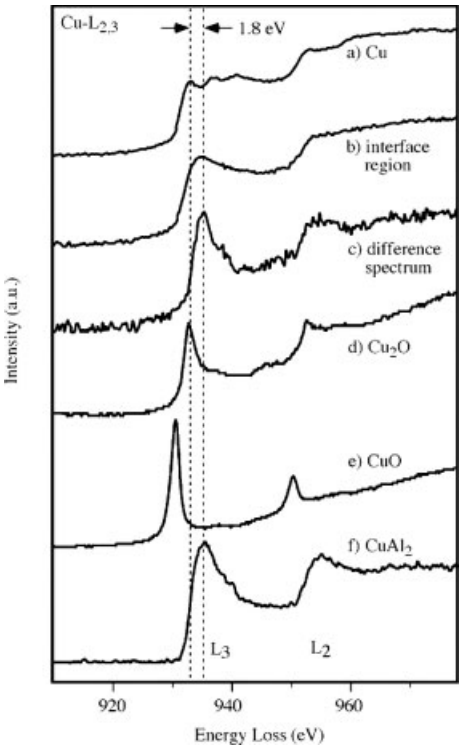

Fig. 12. EELS spectra acquired from the Cu–α-Al_2O_3 interface as presented in Figure 20, a) from the Cu film, b) from the interface region, and c) the difference spectrum. d–f) Standard spectra acquired from bulk Cu_2O, CuO, and $CuAl_2$, respectively (Spectra courtesy of Dr. C. Scheu and Prof. M. Rühle, Max-Planck Institute für Metallforschung, Stuttgart).

~1.8 eV to higher energy-loss and a prominent peak at the edge onset. The standard spectra from Cu_2O, CuO, and $CuAl_2$ are also shown for comparison. The difference spectrum closely resembles the spectrum of $CuAl_2$, suggesting that the Cu atoms at the interface have a similar electronic structure and environment as in $CuAl_2$.

Using EELS, we have illustrated the sensitivity of near edge fine structures to the valence states of transition metal elements. Energy-filtered imaging by selecting electrons with an energy-loss in correspondence to the near edge structure contains the spatial distribution of the valence states across the region. A typical example is the mapping of sp^2 and sp^3 bonds in diamond-like materials.[66] Figure 13 shows an EELS spectrum acquired from CoO that clearly indicates the presence of fine structures in the oxygen K-edge, and the split white lines in the Co L-edge. The relative intensities of the Co-L_3 and Co-L_2 white lines strongly depend on the valence state of cobalt. The ratio L_3/L_2 image gives the distribution of valence states across the specimen.[67–69] Using the images acquired from the white lines, an experimental approach has been demonstrated to map the valence state distributions of Co (or Mn) using energy-filtered electron microscopy.[70,71]

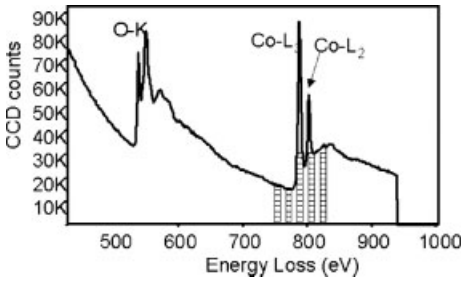

Fig. 13. EELS spectrum acquired from CoO, showing the O-K and Co-L ionization edges.

An energy filtered image can display solid state effects. Figure 14 shows a group of energy-filtered TEM images from a triple point in a CoO–Co_3O_4 two-phase specimen. Chemical images from the O K- and Co L-edges directly reflect the thickness-projected distribution of oxygen and cobalt, respectively (Figs. 14a,b). The Co L_3/L_2 white line ratio image was calculated based on the experimental images recorded using the L_3 and L_2 edges, after subtracting the contribution from the continuous energy-loss region that is due to single atom scattering; the image clearly displays the distribution of cobalt valence states (Fig. 14c). The region with lower oxidation state (Co^{2+}) shows stronger contrast, and the ones with high oxidation states show weaker contrast. The thickness-projected atomic ratio O/Co image was calculated from the im-

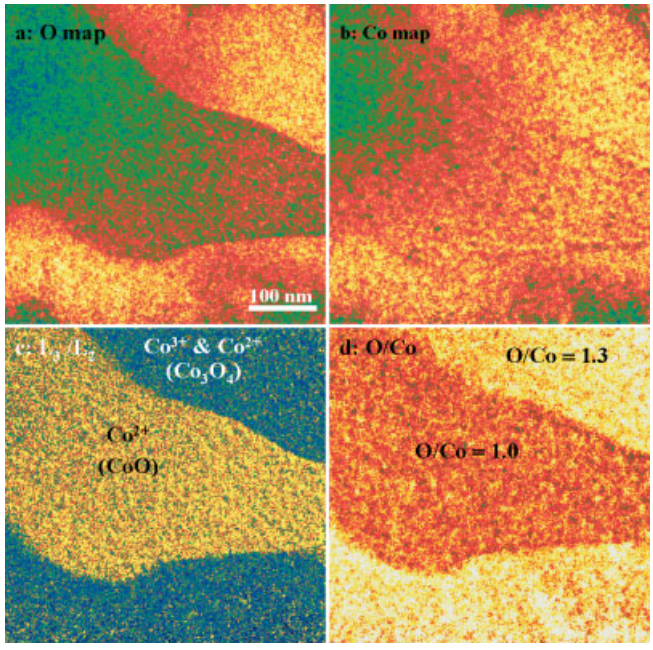

Fig. 14. A group of images recorded from the same specimen region using signals from a) the O K-edge, b) the Co L-edges, c) the processed L_3/L_2 image, displaying the distribution of the valence states. d) The atomic concentration ratio image of O/Co. The continuous background contributed from the single atom scattering has been removed from the displayed Co-L_3 and Co-L_2 images. The O/Co image is normalized with reference to the standard composition of CoO for the lower portion of the image in order to eliminate the strong influence on the ionization cross-section from the white lines.

ADVANCED MATERIALS

ages recorded from the O K-edge and the $L_3 + L_2$ white lines (Fig. 14d). Although the energy-filtered O K-edge image exhibits some diffraction contrast and thickness effect, the O/Co compositional ratio image greatly reduces this effect. The high intensity region in the O/Co image indicates higher local concentrations of oxygen (e.g., higher Co oxidation states), the low intensity region contains comparatively less oxygen (e.g., lower Co valence state), entirely consistent with the information provided by the L_3/L_2 image. A spatial resolution of ~2 nm has been achieved. This is remarkable in comparison to any existing techniques.

The chemical imaging is sensitive to the transition in valence states. In reference to our studies of thermal induced transition metal oxides,[72] a reduction of MnO_2 was carried out in-situ in vacuum at a temperature of 350 °C, and the resulting reduced phases were a mixture of oxides of Mn with valences of 2+, 3+, and 4+. Figure 15 shows a series of images acquired by selecting the different energy-loss signals in EELS. Looking at the conventional bright-field image given in Figure 15a, the crystal appears to be a single piece without typical characters. Energy-filtered images using the Mn L_2- and Mn L_3-lines (Figs. 15b,c) show distinct differences in intensity distribution. After subtracting the image formed by the continuous energy-loss past the L_2 white line, a ratio image of L_3/L_2 is attained (Fig. 15d). A line scan across the image with an average of 50 pixels in width is given below the L_3/L_2 image, in which the distributions of Mn^{4+}, Mn^{2+}, and Mn^{3+} are unambiguously displayed. The reduction of oxides first occurs at the surface region because of the easy desorption of the oxygen, while the core of the crystal is still MnO_2. This type of imaging is powerful in analysis of Co- and Mn-based oxides.

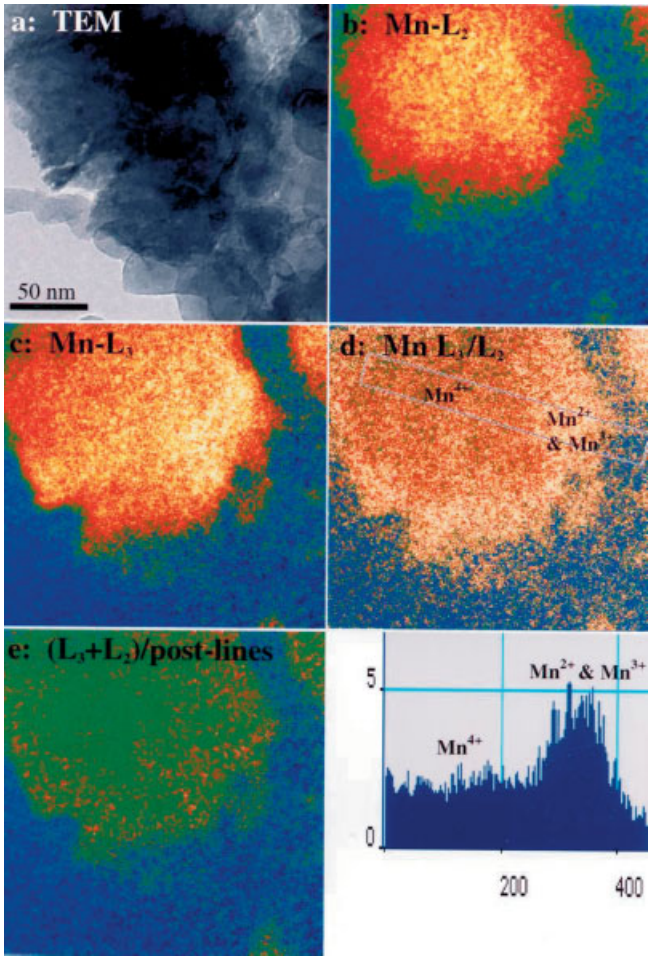

Fig. 15. A group of energy-filtered images acquired from the same specimen region of mixed phases of MnO_2 and Mn_3O_4. a) The conventional bright-field TEM image, b,c) the energy-filtered TEM images of Mn-L_2 and Mn-L_3 white lines, respectively, d) the calculated Mn L_3/L_2 ratio image, and e) the normalized $(L_3 + L_2)$/post-line image. A pixel averaged line scan of the L_3/L_2 ratio from (d) is also given, from which the distribution of Mn^{4+}, Mn^{3+}, and Mn^{2+} are identified.

Using the fine electron probe, valence excitation in multi-walled and single-walled carbon nanotubes have been studied.[73,74] The electron probe can be focused at specific position in reference to the center of the object; the dielectric excitation in a small region of a few nanometers can be investigated. Theoretical calculation based on quasi-classical electron energy loss theory gives a good interpretation of the observed data.

4. Quantitative Microscopy and Electron Diffraction

4.1. Dark-Field Imaging of Small Clusters and Point Defects in STEM

Imaging in the TEM is mainly dominated by elastic scattering, and diffraction effects are highly pronounced if the images are formed by Bragg reflected beams. Bright-field imaging is dominated by diffraction and phase contrast, and is not very sensitive to differences in atomic number. A monolayer HgS grown on the surface of a CdS nanocrystal, for instance, cannot be easily imaged by HRTEM. To reduce the diffraction effect and enhance chemical sensitivity, a dark-field imaging technique has been developed. We now examine the scattering behavior of a single atom, whose scattering factor is given by the Mott formula

$$f_e(s) = e[Z - f_x(s)]/16\pi^2\varepsilon_0 s^2, \quad (5)$$

where f_x is the X-ray scattering factor of the atom, Z its atomic number, and s a variable related to the scattering angle by $s = \sin\theta/\lambda$, where λ is the electron wavelength. Taking the case of large angle scattering with large s, $f_e(s) \approx eZ/16\pi^2\varepsilon_0 s^2$, is directly proportional to the atomic number. This means that atomic number information can be revealed by collecting the signals scattered to high angles. This is done in scanning transmission electron microscopy (STEM) using a high-angle annular dark-field (HAADF) detector to detect the electrons scattered to high angles. This technique was first demonstrated by Crewe for direct imaging of a single gold atom.[75] Figure 16 shows the scattering geometry of a fine electron probe across a specimen in STEM. An HAADF detector is placed

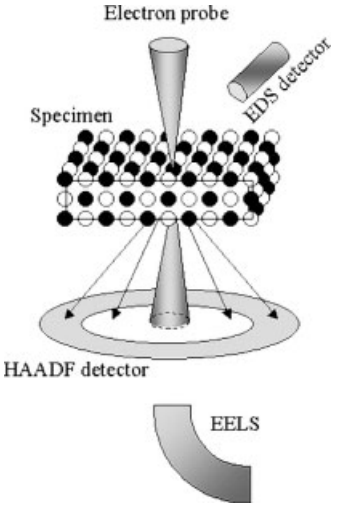

Fig. 16. Scattering geometry in STEM and the corresponding image formation process.

at the diffraction plane that detects the electrons scattered to high angles.

For crystalline specimens, phonon scattering (thermal diffuse scattering, or TDS), which was first proposed by Wang and Cowley[76] as the dominant contributor for HAADF STEM imaging, is the main contributor to scattering to high angles. Details about thermal diffuse scattering can be found elsewhere.[12] The intensity contributed by a single atom at high scattering angle is

$$I_{\mathrm{TDS}}(s) = [f_{\mathrm{e}}(s)]^2 [1 - \exp(-2Ws^2)] \quad (6)$$

where W is the Debye-Waller factor that is sensitive to specimen temperature. $I_{\mathrm{TDS}}(s)$ is proportional to Z^2 at high scattering angle. Since the vibration of the nuclei is responsible for TDS, phonon scattering is a very localized scattering process. The resolution of HAADF STEM is approximately determined by the size of the electron probe.

TEM is a powerful technique for imaging the projected particle shapes and surface atom arrangement through profile imaging.[77] Imaging of surface adsorbed atoms on a nanoparticle, however, can never be an easy task. Due to the rotation of the particle under the scanning tip, direct resolution of the adsorbed atoms by scanning tunneling microscopy is in practice difficult to achieve. Structure analysis of heterocatalysts is a challenge because of strong effects of the substrate. The strong scattering from the substrate greatly reduces the signal from the supported catalyst particles. Conventional high-resolution TEM is dominated by the scattering from the substrate and is insensitive to the adsorbed atom, especially lighter elements. Using HAADF-STEM, the signal from the catalyst particles can be enhanced by the stronger scattering power of the adsorbed atoms. This study has been demonstrated for platinum and rhodium atoms dispersed on γ-Al_2O_3 supports.[78] The configuration of the metal atom cluster could be constructed from the image and a model for surface adsorption could be proposed.

In many cases, it is believed that the surfaces of small particles are the most active sites for catalysis. In practice, besides the small particles, single atoms may be deposited on the substrate surface, which may also be active sites for catalysis. However, the classical technique was unable to observe single atoms due to the strong effect from the substrate. Using HAADF STEM, individual single atoms can be imaged unambiguously. Shown in Figure 17 is a HAADF STEM image of single La atoms on a γ-alumina support recorded at 300 kV with a C_s-corrected electron probe. This is an important advance for studying nanostructured catalysts. A histogram of the full width at half maximum (FWHM) of intensity profiles

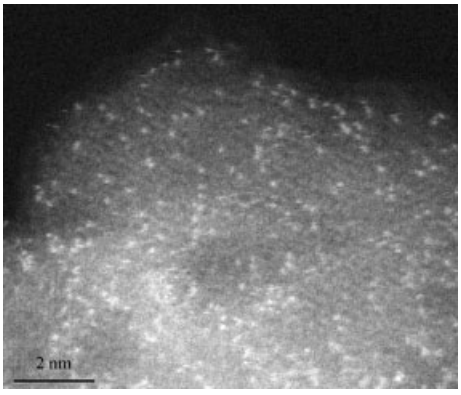

Fig. 17. HAADF STEM image (Z-contrast image) recorded at 300 kV from single La atoms supported on γ-alumina substrate, showing greatly enhanced contrast with the improvement in electron probe size (Image courtesy of Dr. S. J. Pennycook, Oak Ridge National Laboratory).

across single La atoms gives the probe FWHM as about 0.7–0.8 Å. The smaller probe also gives a greatly improved image of the alumina itself. Very faint lattice fringes can be identified in the image.

Imaging of line and planar defects is the most conventional application of TEM. Analysis of point defects, however, is probably the most challenging task. For points distributed with short-range ordering, electron diffraction can be applied to determine the correlation among point defects. If the point defects are distributed randomly, TEM can hardly provide any useful information about point defects because of the difficulty in isolating the information from the defect site from the huge contribution of the diffraction of the main crystal as well as the surface atoms. Recently, Voyles et al. have demonstrated direct imaging of individual Sb dopant atoms in crystalline Si lattice using HAADF STEM.[79] Doping is a conventional processing technique in semiconductor industry. The carrier introduced by dopants is usually described based on statistics because the doping level is typically a few parts per million (ppm). Low doping in nanocrystals could be different because each particle, on average, may have only one or even less than one doping atom. Thus, the question is whether the dopants are located inside the particle or on the surface of the particle? The HAADF-STEM image may provide a possible technique for studying dopants in a single particle if the dopants are heavier atoms.

ADVANCED MATERIALS

4.2. Holography for Imaging Magnetic Nanostructures

Imaging of magnetic domains and interdomain interactions is vitally important for understanding the behavior, improving the properties, and device designing of magnetic materials. The most frequently used techniques for imaging domain structures are Fresnel contrast and Lorentz microscopy (see literature[80] for recent progress) and off-axis electron holography.[81] A comprehensive review of the imaging techniques for magnetic structures can be found elsewhere.[82] This section mainly focuses on the introduction of off-axis electron holography for imaging magnetic structures. The mechanism of imaging magnetic domains in magnetic materials relies on the Aharonov–Bohm effect, which describes the relative phase shift of two electron waves traveling from a point along two routes enclosing a zone with magnetic field distribution to the same point,

$$\Delta\phi = \frac{2\pi e}{h}\int B \cdot dS \tag{7}$$

where dS is a surface integral over the surface area enclosed by the two routes. A key step in observation of magnetic flux lines is to create a magnetic field-free zone in which the specimen to be examine is placed. This can be achieved using a Lorentz objective lens. Electron holography can be applied to image magnetization in magnetic particles, flux lines in superconductors, and magnetic domains in thin films.[83]

The principle of electron holography was first introduced by Gabor[84] in an attempt to exceed the point-to-point resolution of an electron microscope. Holography is based on the interference and diffraction properties of waves, thereby producing a true image of an object (including amplitude and phase) without any distortion of the lenses. The development of high-brightness, high-coherence electron sources has made it possible to obtain holograms using electron waves in TEM.[85–87]

Electron holography is designed as a two-step imaging technique. The first step is to form an interference hologram as shown in Figure 18a. The other step is to reconstruct the hologram to get the real object image. A high-brightness, high coherence electron beam is generated by a field emission source with an energy-spread smaller than 0.5 eV. The specimen is positioned to cover half of the image plane, leaving the other half for the reference wave. The off-axis holograms are recorded by means of an electron biprism inserted between the back focal plane of the objective lens and the intermediate image plane. By applying a positive voltage to the filament of the biprism, the waves on both sides of the biprism are deflected towards each other, forming an interference pattern in the image plane, i.e., the hologram. The two waves passing by the biprism are analogous to the waves emitted by the double slits in the Young's interference experiments in optics. In the second step, as shown in Figure 18b, the goal is to retrieve the amplitude and phase information contained in the hologram. This procedure can be done optically using an interferometer, or by numerical calculation. This step removes the spherical

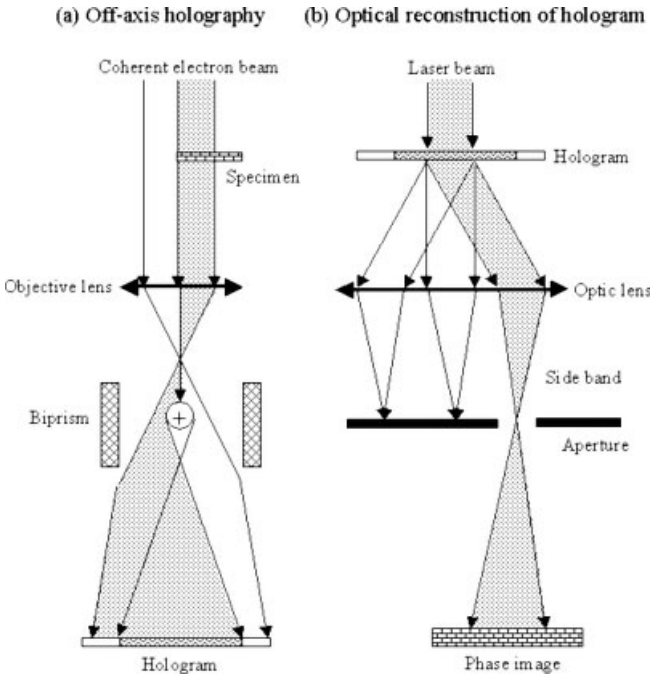

Fig. 18. a) Formation of electron holograms in TEM using an electron biprism; b) reconstructing the amplitude and phase information from the electron hologram.

aberration effect and the defocus introduced by the objective lens, thus, the true phase of the electron wave is retrieved.

Figure 19 shows a phase image of a Co nanoparticle of size ~200 nm, where the contour lines in the interference micrograph directly indicate the magnetic lines of force in h/2e

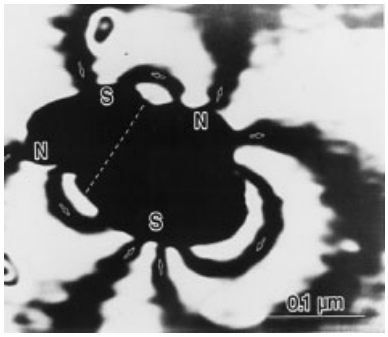

Fig. 19. Electron phase map reconstructed from a holographic image of a plate Co particle (Courtesy of Dr. A. Tonomura, Hitachi).

units.[86] The magnetization direction is clockwise or counterclockwise corresponding to the wave-front protruding like a mountain or a valley. Electron holography is a powerful technique for quantitative analysis of magnetic domain structures.

4.3. Quantitative Electron Diffraction for Refining Atomic Structure and Charge Density Distribution

Analogous to X-ray diffraction, refinement of crystal structure using electron diffraction has been a goal for scientists. It is known that HRTEM imaging is limited and distorted by

aberrations of the objective lenses, but electron diffraction is aberration free. Quantitative analysis of electron diffraction data is rather challenging due to strong electron–specimen interaction that results in dynamic diffraction effects, which has to be quantified by solving the Schrödinger equation. On the other hand, by taking advantage of the strong electron–atom interaction for high-energy electrons, the diffraction intensity is sensitive to charge redistribution in crystalline specimens. Thus, a quantitative fitting of the experimental data with the calculated data produces the charge transfer and bonding maps in functional oxides.[88,89] This study is feasible for perfectly crystalline specimens without defects and surface effects, but its applications for nanomaterials has not been demonstrated as of now.

Surface/interface structure is likely to be the most pronounced structural character of nanomaterials. Studying bonding in inorganic solids is important in understanding many of their properties. Our common knowledge is that metals have metallic bonds and ceramics have covalent and/or ionic bonds. At an interface between metal and ceramics, such as in Nb–Al_2O_3, what is the bonding type? This type of study has been systematically carried out by Rühle's group.[90] They have adopted a first principle calculation of the structure of the interface, which is then used for image calculations based on the well established imaging theory. By systematic comparison between the super quality experimental HRTEM images with the theoretically calculated results, the theoretical model is refined, and thus the interface structure is revealed.

Figure 20 shows a HRTEM image recorded from the interface between Cu and α-Al_2O_3.[65] The orientation relationship

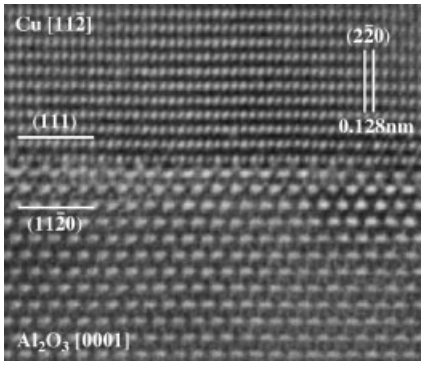

Fig. 20. High-resolution TEM image recorded from the interface between Cu and α-Al_2O_3. The incident beam is [112] Cu and the image was recorded using a 1250 kV atomic resolution TEM with a point-to-point resolution of 0.12 nm (Image courtesy of Dr. C. Scheu and Prof. M. Rühle, Max-Planck Institute für Metallforschung, Stuttgart).

between the film and substrate is: $(11\bar{2}0)_{Al_2O_3}$ $[0001]_{Al_2O_3}$ ∥ $(111)_{Cu}$ $[11\bar{2}]_{Cu}$ No strain field indicative of misfit dislocations was observed, the interface is atomically abrupt, and there is no reaction layer. Quantitative interpretation of the image and building the interface atomic structure model depends on image simulation. Based on the well-established dynamic electron scattering theory,[91] the well accepted computer software,[92] and iterative matching between the experimental image and the calculated image based on the proposed model, the atomic structure at the interface is quantitatively refined. Figure 21a reveals a simulated HRTEM image of the interface using an Al-terminated Al_2O_3 model, and the result is inserted in the figure. It was noticed that the calculated image gives a smaller value of 0.08 ± 0.02 nm for the projected Cu–Al distance at the interface, and the visible contrast at the interface is not reproduced in the calculated image. Therefore, the positions of the Al atoms have to be relaxed at the interfacial region, and the model that gives the best fit to the experimental image is given in Figure 21b. This is an excellent example of interface structure refinement using HRTEM.[91]

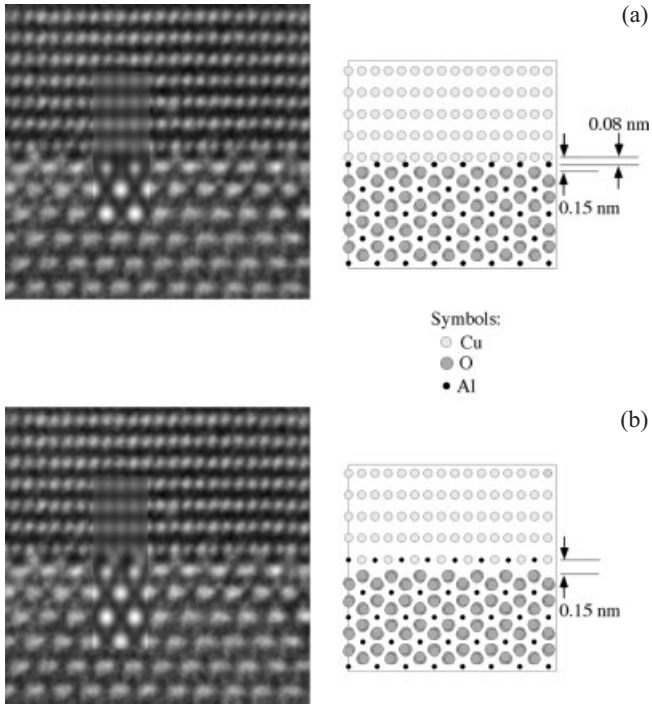

Fig. 21. A quantitative comparison of the high-resolution TEM images recorded from the interface between Cu and α-Al_2O_3 and the calculated images (inserted) based on the model shown on the right-hand side (Image courtesy of Dr. C. Scheu and Prof. M. Rühle, Max-Planck Institute für Metallforschung, Stuttgart).

5. Aberration-Corrected High Resolution Imaging

Due to the imperfection of magnetic lenses, the resolution of the electron microscope is limited by spherical aberration, an effect originating from the dependence of the electron focal length on its scattering angle. There are two typical definitions of resolutions in TEM. The Scherzer resolution or the structural image resolution refers to a resolution at which the images can be directly related to the projected structure of the object, which is given by

$$R_s = (3/4)^{1/2} \lambda^{3/4} C_s^{1/4} \quad (8)$$

where λ is the electron wavelength, and C_s is the spherical aberration coefficient, which is a key quantity in determining

the structural resolution that can be achieved by a TEM. The other resolution is the information limit, which means the finer details presented in the image that might exceed the Scherzer resolution but may not have a direct relationship with the structure of the sample. To enhance the structure image resolution as stated in Equation 8, the classical technique is to reduce the wavelength of the electrons, which means a great increase in the acceleration voltage of the microscope to a range of over one million volts.[93] The consequence of raising acceleration voltage is not only a gigantic increase in cost of manufacturing, operation, and maintenance, but also enhanced radiation damage due to the high energy electrons. An alternative approach is to reduce the spherical aberration coefficient by introducing an aberration corrector around the objective lens, a so-called C_s-corrector. The advantage of using a C_s-corrector is that a sub-angstrom resolution can be achieved while the microscope is operated at lower voltage such as 200 kV. This offers a great advantage for materials analysis.

Correcting the aberration and extending the image resolution have been a constant effort for scientists. The most classical technique is electron holography, as demonstrated by Lichte's group.[94] Electron holography gives the possibility of retrieving electron wave functions at the image plane, which includes the amplitude and phase images. If the experimental parameters such as objective lens defocus Δf and C_s are precisely known, the aberration introduced by the objective lens can be eliminated from the electron wave, thus the true wave function at the exit face of the specimen is received.

In hardware, great and fast progress has been made in the last few years on C_s-corrected TEM, a resolution of better than 0.1 nm has been achieved at 200 kV, while such a resolution requires 1250 kV without the use of a C_s-corrector. There are several approaches having been developed for correcting the C_s. Urban and co-workers[95] have used a hexapole corrector system, which improved the point resolution for a 200 kV TEM from 0.24 nm to 0.14 nm. Krivanek et al.[96] developed a quadrupole–octupole corrector for improving the probe size of a scanning transmission electron microscope.

An improvement in resolution provides following advantages for nanotechnology. Firstly, high quality experimental data is provided for quantitative structure analysis. Secondly, light elements, such as oxygen[97] in functional oxides and even lithium[98] in battery materials, can be directly resolved by TEM. Thirdly, it gives the possibility of increasing the gap between the pole pieces of the objective lens, thus scanning probe techniques and in-situ techniques can be integrated with TEM, and more innovative measurement tools can be used in conjunction with TEM. Finally, a fine and bright electron probe can be formed for atomic resolution spectroscopy and chemical analysis (see Sec. 6).

Structure determination for light elements is usually performed using neutron diffraction because of the significantly larger scattering cross-section. For function oxides that have an ordered distribution of oxygen vacancies, electron diffraction can be applied to determine the structure of the crystal (see Ch. 4 in Wang and Kang[7]). Direct imaging of light elements by electron microscopy has been demonstrated by the C_s-corrected HRTEM very recently.[97] Figure 22A shows an experimental image recorded from a chemically non-stoichiometric $SrTiO_{3-x}$ that has oxygen vacancies. Based on the model inserted in Figure 22A, the projected intensity at the oxygen positions should be equal, but the image, as illustrated by the line scan across atom columns 1 and 2, indicate lower intensity in comparison to the neighbor oxygen columns. Quantitative image calculation by introducing oxygen deficiency for 85 % and 80 % oxygen occupancy in columns 1 and 2, respectively, matches the observed image. This is a beautiful example demonstrating direct imaging of ordered oxygen deficiencies in oxides.[97] It is known that the properties of function oxides are determined by the oxygen deficiency. ZnO, for example, can be tuned from semiconductor to conductor simply by introducing oxygen deficiencies into the lattice. The entire series of Ce-, Pr-, and Tb-based oxides have a wide range of stable homologous phases when ordered oxygen vacancies are introduced.[7] Quantitative determination of light elements using electron based techniques is a key progress in nanomaterials analysis.

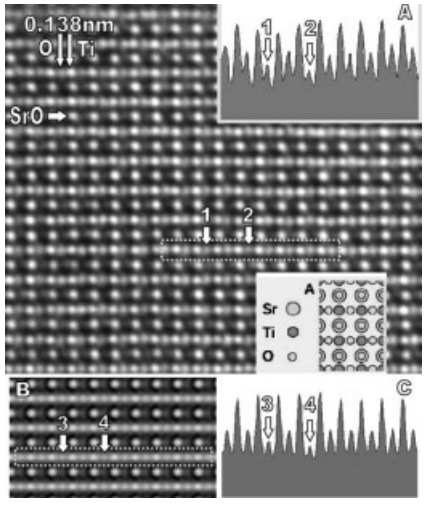

Fig. 22. A) Experimental image of $SrTiO_3$ oriented along [011] using a C_s-corrected high-resolution TEM. The spherical aberration coefficient was adjusted to $C_s = -40$ μm, and the overfocus $\Delta f = 8$ nm. The atomic columns in the projected direction shows bright contrast, and the oxygen atoms are clearly resolved. The intensities in columns 1 and 2 are lower than the neighboring oxygen columns due to the presence of oxygen deficiency. B) Simulated images based on a model for introducing 85 % and 80 % occupancies in the columns 3 and 4, respectively, for oxygen occupancy, shows excellent agreement with the experimental image as indicated by the line trace (Image courtesy of Prof. K. Urban and Dr. C. L. Jia, Institute of Solid State Research, Jülich).

Among the list for light elements in solid materials, hydrogen, lithium, beryllium, boron, carbon, nitrogen, and oxygen are the most important members. Recent experiments by Shao-Horn et al.[98] have shown the direct imaging of lithium atoms in battery materials. Figure 23 shows the HRTEM image recorded from $LiCoO_2$, where the projected positions of the oxygen, cobalt, and lithium atoms are indicated. It is apparent that Li atoms are clearly resolved for the first time by

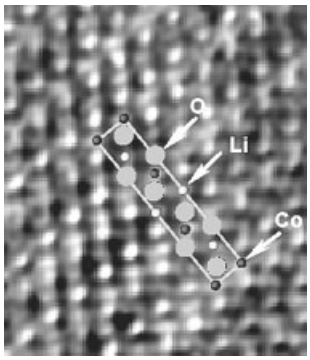

Fig. 23. Sub-angstrom image of $LiCoO_2$ battery material from Shao-Horn et al. [98] shows all atom species. As indicated by the superimposed model, the strong white peaks occur at the positions of oxygen atom columns, the strong fuzzy peaks at cobalt sites, and the weak white peaks show lithium positions. The authors confirmed the identities of the peaks with image simulation. (Reprinted with permission; copyright Nature Publishing Group 2003).

electron imaging. This exciting advance will no doubt be a great boost in the research and development of nanoscale energy storage materials.

Aberration correction can also be carried out by image processing, which has been systematically developed by Van Dyck's group.[99] An important variable that can be changed in recording electron images is the objective lens focus. If a focus series of HRTEM images is recorded from the same specimen area, the nonlinear information transfer function of the optical system can be corrected and the complex wave function at the exit face of the specimen can be retrieved by image processing. This process requires high stability of the microscope and image drift correction. A large improvement in image resolution has been achieved.

6. Sub-Angstrom Electron Probe and Single Atom Detection

A unique advantage of chemical imaging in STEM is that the spatial resolution is solely determined by the size of the electron probe for very thin specimens. In STEM, the electron-specimen interaction occurs after the formation of the electron probe by the condenser lens, thus, the chromatic aberration effect arising from inelastic interaction is eliminated, a major advantage over TEM. Therefore, the broadening of the electron probe as a result of electron energy-loss is solely determined by angular broadening introduced by the intrinsic physics, the enlargement from the lens is diminished. By considering the high localization of the inner shell ionizations of atoms, it is possible to achieve atomic resolution chemical analysis and imaging in STEM.[100]

For a C_s-limited STEM, the optimum electron probe size is given by

$$d_p = 0.4\,\lambda^{3/4}\,C_s^{1/4} \tag{9}$$

A correction in C_s means a great improvement in probe size. Krivanek et al.[96] have developed a quadrupole–octupole corrector for improving the probe size of a 100 kV STEM to 0.1 nm,[101] which has been applied to image gold nanocrystals at a resolution of 0.1 nm.[102]

Cowley has proposed a new approach that can achieve a probe size of 0.05 nm without using the C_s corrector.[103] The approach is based on the atom lens, in which a heavy atom, placed in front of an electron probe in STEM, could focus the electron probe to a size of ~0.05 nm. Experiments on carbon shell have demonstrated the feasibility of this proposal.[104,105]

Spectrum-imaging of single atoms in STEM must overcome several hurdles. The *S*/*N* ratio, which is affected by the ionization cross-section of the element to be detected and the thickness of the substrate, which is usually carbon. The beam dose is also important. Radiation damage, particularly to light elements and biological specimens, is a main concern, which is likely to induce structural degradation, atom diffusion, and limited data acquisition time. Specimen drift must be minimized to extend the data acquisition time. It is now possible to digitally correct the drifting effect. As the size of the electron probe is approaching 0.1 nm, a single light atom can be identified. Leapman and Rizzo[106] have successfully imaged two phosphorus atoms using EELS. Single atom imaging has recently been demonstrated by Suenaga et al.[107] who imaged a Gd atom trapped in a C_{60} molecule. The C_{60} molecules are aligned as a chain inside a single-walled carbon nanotube, and each C_{60} molecule is the cage for storing one Gd atom.

Using a fine electron probe, local electronic structure can be examined with atomic resolution. With the improvement in instrumentation, it is anticipated that EELS can be acquired at an energy-resolution of better than 0.1 eV at a spatial resolution better than 0.1–0.2 nm. Such a dramatic performance of the future EELS is likely to significantly impact the nanoscale chemical and electronic analysis in the following aspects. Firstly, with an ultra small electron probe, chemical analysis and local electronic structure can be quantitatively detected from a single atomic column. This provides a novel technique for probing the solid state structure, column-by-column, allowing a direct probe of the local density of states at a defect site, the atoms at interfaces and at grain boundaries. This is vitally important for understanding the impurity states introduced by defects and the local bonding transformation at interfaces. Secondly, chemical analysis with atomic resolution provides an effective approach for "atom-by-atom" nanoengineering. Finally, chemical imaging towards atomic resolution has a vast impact for solving many problems in materials science. It could provide a powerful approach for identifying point defects, grain boundary segregation, interface reaction and diffusion, and impurities at defect sites, etc.

7. Sub-eV Resolution Spectroscopy

The energy resolution in TEM is in the order of 0.5–1 eV. To be adequate for resolving solid state electron structure, a resolution of better than 0.1 eV is required. The energy spread of a field emission source is 0.5–0.7 eV. A major effort

in microscopy now is to develop a monochromator that refines the energy spread of the electron beam that transmits the specimen to an order of 0.1 eV. With the proposed energy resolutions one has the potential to examine local mechanical, thermal, and acoustic processes. Phonon excitation in the bulk and at the surface is an outstanding example. If it would be possible to observe phonon excitations at a spatial resolution at the atomic level, the structural stability of atoms at interfaces and defects could be detected. For instance, in materials that undergo certain structural phase transitions, the onset of the transition is signaled by a softening of the structure. This softening is detectable by observation of phonon modes.

7. Creation of Nanoscale Structures by a Fine Electron Probe

Nanoscale patterns can be fabricated by an electron beam. Radiation damage by an electron beam is dominated by three processes: breaking bonds by knock-on collision with the atoms, ionization of inner shell electrons, and local heating. It is known that some of the materials are sensitive to electron beam illumination, and their structures change under the electron beam. Using this characteristic, a fine electron probe in STEM can be useful for creating nanoscale patterns. It was reported by Humphreys et al.[108] that an electron beam in STEM can drill a nanometer size hole through a MgO cube. α-Al_2O_3 can be reduced into metallic Al by a strong electron beam.[109] The mechanism of this radiation damage is attributed to an internal Auger decay process. Figure 24 shows an image of an AlF_3 cube prior and after scanning an electron beam across its surface, resulting in the formation of a metal wire, as indicated.[110] The metal nanowire is metallic Al because AlF_3 can be easily reduced by the electron beam. The width of the Al nanowire could be controlled by choosing the size of the electron beam, the acceleration voltage and the beam radiation time.

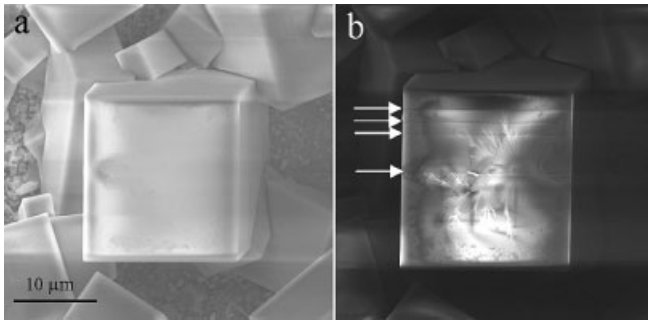

Fig. 24. Scanning electron microscopy images of AlF_3 cube synthesized by a solid-vapor process, a) before and b) after scanning an electron beam slowly along the line indicated, showing the formation of wire in the sample.

It is known that some precursors can be dissociated by an electron beam even at low temperatures, thus thin films can be made by electron-beam assisted chemical vapor deposition. Using a fine electron probe in STEM, patterned structures can be fabricated by controlling the scan of the electron probe with the presence of the chemical vapor.

8. Summary and Perspectives

This paper reviews some of the most recent progress in electron microscopy techniques for nanotechnology. Based on existing experiments, the review focuses on novel approaches that have been demonstrated for solving problems in nanomaterials. The review covered the following areas: in-situ microscopy, in-situ nanoscale property measurements, environmental microscopy, angstrom-resolution imaging, high-angle annular-dark-field STEM imaging, electron holography, and high-spatial resolution EELS. The reviewer believes that these areas will be the future directions of electron microscopy for nanotechnology.

Understanding atomic structure, detecting local chemistry, measuring local electronic structure, and probing local properties are essential in "atom-by-atom" engineering for nanotechnology. Picometer-scale imaging provided by TEM is essential for nanometer-scale technology. It is apparent that atom-by-atom engineering is the state of the art for nanoscience, but it may not be practical for nanotechnology to meet the need of mass production with extremely high reproducibility. We are convinced that self-assembly will be the fundamental of nanotechnology, just like the self-assembly process in biosystems. Self-assembly will be the bridge that links the "bottom–up" with the "top–down" approaches for nanotechnology. Understanding the column-by-column atomic structure, properties and manipulation are the first steps for controlling the self-assembly process of future nanomaterials and processing. Electron microscopy will be indispensable and crucial for bringing the blueprint of nanotechnology to reality.

Received: March 18, 2003
Final version: June 6, 2003

[1] *Research Horizon* (Ed: J. M. Sanders), Georgia Tech, Atlanta, GA **2001**, p. 5.
[2] Z. L. Wang, Y. Liu, Z. Zhang, *Handbook of Nanophase and Nanostructured Materials*, Vols. I–IV, co-published by Kluwer Academic Press, New York, and Tsinghua University Press, **2002**.
[3] P. Buseck, J. M. Cowley, L. Eyring, *High Resolution Transmission Electron Microscopy: Theory and Applications*, Oxford University Press, New York **1989**.
[4] G. G. Tibbetts, *J. Cryst. Growth* **1984**, *66*, 632.
[5] S. Iijima, *Nature* **1991**, *354*, 56.
[6] Z. L. Wang, C. Hui, *Electron Microscopy of Nanotubes*, Kluwer Academic Publisher, New York **2003**.
[7] Z. L. Wang, Z. C. Kang, *Functional and Smart Materials—Structural Evolution and Structure Analysis*, Ch. 6–8, Plenum Press, New York **1998**.
[8] Z. L. Wang, *J. Phys. Chem. B* **2000**, *104*, 1153.
[9] Z. L. Wang, *Adv. Mater.* **1998**, *10*, 13.
[10] Z. L. Wang, Z. R. Dai, S. Sun, *Adv. Mater.* **2000**, *12*, 1944.
[11] D. B. Williams, C. B. Carter, *Transmission Electron Microscopy*, Plenum Press, New York **1996**.
[12] Z. L. Wang, *Elastic and Inelastic Scattering in Electron Diffraction and Imaging*, Plenum Press, New York **1995**.
[13] L. Reimer, *Transmission Electron Microscopy*, 3rd ed., Springer-Verlag, New York **1993**.
[14] P. Buffat, J.-P. Borel, *Phys. Rev. A* **1976**, *13*, 2287.
[15] Z. L. Wang, J. Petroski, T. Green, M. A. El-Sayed, *J. Phys. Chem. B* **1998**, *102*, 6145.

[16] T. S. Ahmadi, Z. L. Wang, T. C. Green, A. Henglein, M. A. El-Sayed, *Science* **1996**, *28*, 1924.
[17] Y. H. Gao, Y. Bando, *Nature* **2002**, *415*, 599.
[18] For a review see Z. L. Wang in *Electron Microscopy of Nanotubes* (Eds: Z. L. Wang, C. Hui), Kluwer Academic Publisher, New York **2003**, Ch. 7.
[19] R. Berger, C. Gerber, H. P. Lang, J. K. Gimzewshi, *Microelectron. Eng.* **1997**, *35*, 373.
[20] G. H. Wu, R. H. Datar, K. M. Hansen, T. Thundat, R. J. Cote, A. Majumdar, *Nat. Biotechnol.* **2001**, *19*, 856.
[21] K. A. Stevenson, A. Mehta, P. Sachenko, K. M. Hansen, T. Thundat, *Langmuir* **2002**, *18*, 8732.
[22] G. Abadal, Z. J. Davis, B. Helbo, X. Borrise, R. Ruiz, A. Boisen, F. Campabadal, J. Esteve, E. Figueras, F. Perez-Murano, N. Barniol, *Nanotechnology* **2001**, *12*, 100.
[23] Z. J. Davis, G. Abadal, O. Khn, O. Hansen, F. Grey, A. Boisen, *J. Vac. Sci. Technol. B* **2000**, *18*, 612.
[24] Z. W. Pan, Z. R. Dai, Z. L. Wang, *Science* **2001**, *291*, 1947.
[25] M. H. Huang, M. H., S. Mao, H. Feick, H., Yan, Y. Wu, H. Kind, E. Weber, R. Russo, P. Yang, *Science* **2001**, *292*, 1897.
[26] M. S. Arnold, P. Avouris, Z. W. Pan, Z. L. Wang, *J. Phys. Chem. B* **2003**, *107*, 659.
[27] E. Comini, G. Faglia, G. Sberveglieri, Z. W. Pan, Z. L. Wang, *Appl. Phys. Lett.* **2002**, *81*, 1869.
[28] Y. Cui, Q. Wei, H. Park, C. M. Lieber, *Science* **2001**, *3*, 1289.
[29] M. K. Gudiksen, L. J. Lauhon, J. Wang, D. C. Smith, C. M. Lieber, *Nature* **2002**, *415*, 617.
[30] H. G. Craighead, *Science* **2000**, *290*, 1532.
[31] W. Hughes, Z. L. Wang, *Appl. Phys. Lett.* **2003**, *82*, 2886.
[32] P. Poncharal, Z. L. Wang, D. Ugarte, W. A. de Heer, *Science* **1999**, *283*, 1513.
[33] Z. L. Wang, P. Poncharal, W. A. de Heer, *Pure Appl. Chem*. **2000**, *72*, 209.
[34] R. P. Gao, Z. L. Wang, Z. G. Bai, W. de Heer, L. Dai, M. Gao, *Phys. Rev. Lett.* **2000**, *85*, 622.
[35] Z. L. Wang, Z. R. Dai, Z. G. Bai, R. P. Gao, J. Gole, *Appl. Phys. Lett*. **2000**, *77*, 3349.
[36] X. D. Bai, E. G. Wang, P. X. Gao, Z. L. Wang, *Appl. Phys. Lett*. **2003**, *82*, 4806.
[37] L. Meirovich, *Elements of Vibration Analysis*, 2nd ed., McGraw-Hill, New York **1986**.
[38] D. Qian, E. C. Dickey, *J. Microsc. (Oxford)* **2001**, *204*, 39.
[39] E. A. Stach, T. Freeman, A. M. Minor, D. K. Owen, J. Cumings, M. A. Wall, T. Chraska, R. Hull, J. W. Morris, A. Zettl, U. Dahmen, *Microsc. Microanal.* **2001**, *7*, 507.
[40] D. Erts, A. Lohmus, R. Lohmus, H. Olin, A. V. Pokropivny, L. Ryen, K. Svensson, *Appl. Surf. Sci*. **2002**, *7699*, 1.
[41] For a review see Z. L. Wang in *Electron Microscopy of Nanotubes* (Eds: Z. L. Wang, C. Hui), Kluwer Academic Publisher, New York **2003**, Ch. 8.
[42] P. Poncharal, C. Berger, Y. Yi, Z. L. Wang, W. de Heer, *J. Phys. Chem. B* **2002**, *106*, 12 104.
[43] S. J. Tans, M. H. Devoret, H. J. Dai, A. Thess, R. E. Smalley, L. J. Geerligs, C. Dekker, *Nature* **1997**, *386*, 474.
[44] Z. L. Wang, P. Poncharal, W. A. De Heer, *Microsc. Microanal.* **2000**, *6*, 224.
[45] S. Frank, P. Poncharal, Z. L. Wang, W. A. De Heer, *Science* **1998**, *280*, 1744.
[46] For a review see Z. L. Wang, in *Electron Microscopy of Nanotubes* (Eds: Z. L. Wang, C. Hui), Kluwer Academic Publisher, New York **2003**, Ch. 9.
[47] R. P. Gao, Z. W. Pan, Z. L. Wang, *Appl. Phys. Lett.* **2001**, *78*, 1757.
[48] Z. L. Wang, *Adv. Mater*. **2000**, *12*, 1295.
[49] X. D. Bai, E. G. Wang, Z. L. Wang, unpublished.
[50] J. Cumings, A. Zettl, *Science* **2000**, *289*, 602.
[51] J. C. H. Spence, W. Lo, M. Kuwabara, *Ultramicroscopy* **1990**, *33*, 69.
[52] Z. L. Wang, *Reflection Electron Microscopy and Spectroscopy for Surface Studies*, Cambridge University Press, Cambridge **1996**.
[53] Y. Kondo, K. Takayanagi, *Science* **2000**, *289*, 606.
[54] H. Ohnishi, Y. Kondo, K. Takayanagi, *Nature* **1998**, *395*, 780.
[55] V. Rodrigues, J. Bettini, A. R. Rocha, L. G. C. Rego, D. Ugarte, *Phys. Rev. B* **2002**, *65*, 153 402.
[56] V. Rodrigues, D. Ugarte, *Nanotechnology* **2002**, *13*, 404.
[57] R. Sharma, *Microsc. Microanal.* **2001**, *7*, 494.
[58] P. L. Gai, *Top. Catal.* **1999**, *8*, 97.
[59] P. L. Gai, *Microsc. Microanal.* **2002**, *8*, 21.
[60] P. L. Gai, *Curr. Opin. Solid State Mater. Sci.* **2001**, *5*, 371.
[61] T. W. Hansen, J. B. Wagner, P. L. Hansen, S. Dahl, H. Topsoe, C. J. H. Jacobsen, *Science* **2001**, *294*, 1508.
[62] P. L. Hansen, J. B. Wagner, S. Helveg, J. R. Rostrup-Nielsen, B. S. Clausen, H. Topsøe, *Science* **2002**, *295*, 2053.
[63] K. Suenaga, C. Colliex, N. Demoncy, A. Loiseau, H. Pascard, F. Willaime, *Science* **1997**, *278*, 653.
[64] K. Suenaga, M. Tencé, C. Mory, C. Colliex, H. Kato, T. Okazaki, H. Shinohara, K. Hirahara, S. Bandow, S. Iijima, *Science* **2000**, *290*, 2280.
[65] J. M. Cowley, A. F. Moodie, *Acta Crystallogr*. **1957**, *10*, 609.
[66] J. Mayer, J. M. Plitzko, *J. Microsc.* **1996**, *183*, 2.
[67] D. H. Pearson, C. C. Ahn, B. Fultz, *Phys. Rev. B*, **1993**, *47*, 8471.
[68] H. Kurata, C. Colliex, *Phys. Rev. B* **1993**, *48*, 2102.
[69] Z. L. Wang, J. S. Yin, Y. D. Jiang, *Micron* **2000**, *31*, 571.
[70] Z. L. Wang, J. Bentley, N. D. Evans, *J. Phys. Chem. B* **1999**, *103*, 751.
[71] Z. L. Wang, J. Bentley, N. D. Evans, *Micron* **2000**, *31*, 355.
[72] Z. L. Wang, J. S. Yin, W. D. Mo, Z. J. Zhang, *J. Phys. Chem. B.* **1997**, *101*, 6793.
[73] T. Stöckli, Z. L. Wang, J.-M. Bonard, P. Stadelmann, A. Châtelain, *Phys. Rev. B* **2000**, *61*, 5751.
[74] T. Stöckli, J.-M. Bonard, A. Châtelain, Z. L. Wang, P. Stadelmann, *Appl. Phys. Lett*. **2002**, *80*, 2982.
[75] A. V. Crewe, *Chem. Scr.* **1978–1979**, *14*, 17.
[76] Z. L. Wang, J. M. Cowley, *Ultramicroscopy* **1989**, *31*, 437.
[77] L. D. Marks, D. J. Smith, *Nature* **1983**, *303*, 316.
[78] P. D. Nellist, S. J. Pennycook, *Science* **1996**, *274*, 413.
[79] P. M. Voyles, D. A. Müller, J. L. Grazul, P. H. Citrin, H.-J. L. Gossmann, *Nature* **2002**, *416*, 826.
[80] Y. Zhu, V. V. Volkov, M. De Graef, *J. Electron Microsc.* **2001**, *50*, 447.
[81] A. Tonomura, *Electron Holography*, Springer-Verlag, New York **1993**.
[82] M. De Graef, Y. Zhu, *Magnetic Imaging and its Applications to Materials*, Academic Press, New York **2000**.
[83] T. Matsuda, S. Hasegawa, M. Igarashi, T. Kobayashi, M. Naito, H. Kayiyama, J. Endo, N. Osakabe, A. Tonomura, *Phys. Rev. Lett.* **1989**, *62*, 2519.
[84] D. Gabor, *Proc. R. Soc. London, Ser. A* **1949**, *197*, 454.
[85] G. Möllenstedt, *Adv. Opt. Electron Microsc.* **1991**, *12, 1.*
[86] A. Tonomura, *Microsc. Soc. Am. Bull.* **1994**, *24*, 501.
[87] H. Lichte, *Adv. Opt. Electron Microsc.* **1991**, *12*, 25.
[88] J. M. Zuo, M. Kim, M. O'Keeffe, J. C. H. Spence, *Nature* **1999**, *401*, 49.
[89] Y. Zhu, L. Wu, J. Tafto, *Phys. Rev. Lett.* **2000**, *85*, 5126.
[90] M. Rühle, *J. Eur. Ceram. Soc.* **1996**, *16*, 363.
[91] C. Scheu, W. Stein, M. Rühle, *Phys. Status Solidi B* **2000**, *222*, 199.
[92] P. Staddelmann, *Ultramicroscopy* **1987**, *21*, 131.
[93] S. B. Lee, W. Sigle, M. Rühle, *Acta Mater.* **2002**, *50*, 2151.
[94] H. Lichte, *Adv. Opt. Electron Microsc*. **1991**, *12*, 25.
[95] M. Haider, H. Rose, S. Uhlemann, E. Schwan, B. Kabius, K. Urban, *Ultramicroscopy* **1998**, *75*, 53.
[96] O. L. Krivanek, N. Dellby, A. R. Lupini, *Ultramicroscopy* **1999**, *78*, 1.
[97] C. L. Jian, M. Lentzen, K. Urban, *Science* **2003**, *299*, 870.
[98] Y. Shao-Horn, L. Croguennec, C. Delmas, E. C. Nelson, M. A. O'Keefe, *Nat. Mater.* **2003**, *2*, 464.
[99] H. W. Zandbergen, D. van Dyck, *Microsc. Res. Tech.* **2000**, *49*, 301.
[100] P. E. Batson, *Ultramicroscopy* **1992**, *47*, 133.
[101] N. Dellby, O. L. Krivanek, P. D. Nellist, P. E. Batson, A. R. Lupini, *J. Electron Microsc.* **2001**, *50*, 177.
[102] P. E. Batson, N. Dellby, O. L. Krivanek, *Nature* **2002**, *418*, 617.
[103] J. M. Cowley, J. C. H. Spence, V. V. Smirnov, *Ultramicroscopy* **1997**, *68*, 135.
[104] J. M. Cowley, *Phys. Rev. Lett.* **2001**, *87*, 016 101.
[105] J. M. Cowley, *Ultramicroscopy* **2000**, *81*, 47.
[106] R. D. Leapman, N. W. Rizzo, *Ultramicroscopy* **1999**, *78*, 251.
[107] K. Suenaga, T. Tence, C. Mory, C. Colliex, H. Kato, T. Okazaki, H. Shinohara, K. Hirahara, S. Bandow, S. Iijima, *Science* **2000**, *290*, 2280.
[108] C. J. Humphreys, I. G. Salisbury, S. D. Berger, R. S. Timsit, M. E. Mochel, *EMAG'85*, *Inst. Phys. Conf. Ser.* **1985**, *78*, 1.
[109] Z. L. Wang, *J. Microsc.* **1991**, *163*, 261.
[110] C. Ma, Y. Berta, Z. L. Wang, *Solid State Commun.*, in press.

